



HAL
open science

Analytical solutions for analysing pumping tests near an infinite vertical and anisotropic fault zone based upon unconventional application of well-image theory

Benoît Dewandel, Vivien Hakoun, Sandra Lanini, Claudine Lamotte,
Jean-Christophe Maréchal

► To cite this version:

Benoît Dewandel, Vivien Hakoun, Sandra Lanini, Claudine Lamotte, Jean-Christophe Maréchal. Analytical solutions for analysing pumping tests near an infinite vertical and anisotropic fault zone based upon unconventional application of well-image theory. *Advances in Water Resources*, 2022, 160, 10.1016/j.advwatres.2021.104107 . hal-03540594

HAL Id: hal-03540594

<https://hal.science/hal-03540594v1>

Submitted on 24 Jan 2022

HAL is a multi-disciplinary open access archive for the deposit and dissemination of scientific research documents, whether they are published or not. The documents may come from teaching and research institutions in France or abroad, or from public or private research centers.

L'archive ouverte pluridisciplinaire **HAL**, est destinée au dépôt et à la diffusion de documents scientifiques de niveau recherche, publiés ou non, émanant des établissements d'enseignement et de recherche français ou étrangers, des laboratoires publics ou privés.

1 **Analytical solutions for analysing pumping tests near an infinite vertical and anisotropic**
2 **fault zone based upon unconventional application of well-image theory**

3 Benoît Dewandel^{*,1,2}, Vivien Hakoun^{1,2}, Sandra Lanini^{1,2}, Bernard Ladouche^{1,2}, Claudine
4 Lamotte¹ and Jean-Christophe Maréchal^{1,2}

5 (1) BRGM, Univ Montpellier, Montpellier, France

6 (2) G-eau, UMR 183, INRAE, CIRAD, IRD, AgroParisTech, Supagro, BRGM,
7 Montpellier, France

8 b.dewandel@brgm.fr; v.hakoun@brgm.fr; s.lanini@brgm.fr, b.ladouche@brgm.fr;
9 c.lamotte@brgm.fr; jc.marechal@brgm.fr

10 * Corresponding author

11

12 **Abstract**

13 We present a new set of analytical solutions for analysing pumping tests in a well near a
14 vertical fault zone, dyke or vein. We consider a fault zone with finite width, storativity and
15 hydraulic conductivity, which can be anisotropic, and without limitation of the diffusivity
16 contrast between the three aquifer domains (pumped aquifer, fault zone and opposite-side
17 aquifer). This configuration, not described before, also considers flow transience within the
18 fault zone. Drawdown solutions were developed for the three-aquifer domains based on an
19 unconventional application of the well-image theory. Their comparison with numerical
20 modelling results was very satisfactory. Drawdown behaviour at the pumping well is
21 discussed for contrasted properties between the three-aquifer domains. Original analytical
22 solutions for transient flow along both sides of the fault zone, and net transient flow from the
23 fault itself, are proposed and discussed, with particular attention to flow reversal, from the
24 pumped compartment to the fault zone, which occurs where the fault zone is the most
25 transmissive. Finally, we extend the solutions to the case of a well intersecting and pumping a
26 vertical fracture of finite length located near the same vertical geological discontinuity.

27

28 **Keywords:** Pumping test, Anisotropic fault, Pumping near a fault, Compartmented aquifer,
29 Analytical solution

30

31 **1. Introduction**

32 In hydrogeology, the oil-and-gas industry, and geothermal activities, well testing is an
33 essential tool for assessing the hydrodynamic properties of a reservoir. The evaluation of
34 these properties, as well as their variability in space, is essential for improving resource
35 management (e.g., Raghavan, 2004; Dewandel et al., 2012). In addition, detailed groundwater
36 flow conditions, particularly in fractured systems, are required for pressure and transfer
37 modelling, for instance in the case of a nuclear-waste deposit, geothermal exploitation, or
38 contaminant transport. Therefore, the design of an adequate conceptual model based on well-
39 test data prior to quantification of the hydrogeologic parameters has been a topic of interest
40 for decades (Bourdet et al., 1983, 1989; Ehlig-Economides, 1988; Renard et al., 2009; Rafini
41 and Larocque, 2012; Ferroud et al., 2019, etc.).

42 A common case encountered in the field is a well located near a fault (Fig. 1a) that may act as
43 a barrier or a conduit, or a combination of both, to flow (e.g., Maslia and Prowell, 1990,
44 Haneberg, 1995, Bense et al., 2003). In sedimentary rock, but not only, faults may be
45 permeable, or act as low- or non-permeable structures, because the throw along the fault plane
46 may be such that a permeable layer on one side of the fault is completely, or partially,
47 juxtaposed against an impermeable layer on the other side, or because of low hydraulic
48 conductivity materials in the core of the fault zone. The reverse is also possible, where the
49 rock's hydraulic conductivity is enhanced because of unaltered fracturing along the fault zone
50 (Caine et al., 1996). Other geological features, such as dykes, veins, or karst conduits, may
51 locally enhance the hydraulic conductivity, and drain the surrounding aquifer, or act as a
52 barrier or low-permeability discontinuity to flow (Dewandel et al., 2011, Perrin et al. 2011;
53 Lachassagne et al., 2011, 2021, Maréchal et al. 2014; Xiong et al., 2017; Xu et al., 2018).

54 Depending upon the properties of the fault or of the geological discontinuity, fluid flow may
55 occur along the structure and across the structure's planes. Several analytical studies have
56 described transient pressure behaviour in the pumping well and flow processes; such work
57 often refers to a pumping well near a fault of infinite length with finite-conductivity
58 (Abbaszadeh and Cinco-Ley, 1995, Abbaszadeh et al., 2000; Escobar et al., 2013). Yaxley
59 (1987) derived an analytical solution from Bixel's et al. (1963) work for a well located near a
60 partially communicating vertical fault. This model, dedicated to low-permeable barrier, does
61 not account for flow along the fault plane. Abbaszadeh and Cinco-Ley (1995) presented a

62 solution for a well located near a finite-conductivity vertical fault, with fracture skin for
63 simulating damage zones on the sides of the fault plane. Their solution allowed varying
64 aquifer properties on both sides of the fault, considered flow along and across the fault plane,
65 but assumed a small fault width and neglected fault storativity and thus flow transience in the
66 fault zone, the net flux in/out of the fault being nil. This model was dedicated to fault zones
67 with higher hydraulic conductivity than those of the surrounding aquifers. Later, Rahman et
68 al. (2003) proposed a semi-analytical solution similar to Abbaszadeh and Cinco-Ley (1995)'s
69 work, to account for transient flow in the fracture plane, but also assumed a greater hydraulic
70 conductivity in the fault. Other solutions exist in the literature, such as that developed by
71 Boussila et al. (2003) for a well near a linear leaky boundary in laterally infinite composite
72 systems, or the one proposed by Althawad (2016) for a pumping well intersecting and
73 pumping a finite conductivity fracture of infinite length near a finite conductivity fracture of
74 infinite length.

75 Vertical faults, or other vertical geological discontinuities, can also be conceptualized as
76 vertically compartmented aquifers. Butler and Liu (1991) and Dewandel et al. (2014),
77 proposed solutions for investigating the influence of a pumping well located in a linear strip
78 aquifer—representing the geological discontinuity—bounded laterally by aquifers of differing
79 properties. However, no analytical solution was provided for a pumping well located in one of
80 the two external compartments and thus near the geological discontinuity. Anderson (2006),
81 using the method of images, presented an analytical solution for a pumping well near such a
82 discontinuity. His solution allows considering the anisotropy in hydraulic conductivity of the
83 central compartment, the one representing a vertical fault zone, or another vertical geological
84 discontinuity. However, this solution was established for steady-state flow only. Rafini and
85 Larocque (2009) used numerical models for assessing the flow behaviour induced by a
86 pumping test near a fault zone, embedded in a low-permeable matrix with various fault
87 inclinations, but they did not consider the anisotropy in hydraulic conductivity of the fault
88 zone.

89 We propose new analytical solutions for drawdown induced by a pumping well near an
90 infinite sub-vertical and anisotropic fault zone (or another vertical geological discontinuity).
91 We consider a fault zone of finite width, storativity and hydraulic conductivity that can be
92 anisotropic (Fig. 1a), without limitation of the diffusivity contrast between the three-aquifer
93 domains (pumped aquifer, fault zone and opposite-side aquifer), which was not considered in
94 earlier works. Our solutions are based upon an unconventional application of the well-image

95 theory. Solutions are first developed for an isotropic fault and then extended to the anisotropic
96 case; they are given for the three-aquifer domains and are compared to numerical modelling.
97 The hydrodynamic signatures of drawdown and flow behaviour at the pumping well are
98 discussed. Analytical solutions for transient flow along both sides of the central compartment
99 (the fault zone) are given in terms of spatial and transient evolution, with particular attention
100 to reversed flow, i.e. flow from the pumped compartment entering the fault zone, which can
101 occur under specific conditions. These new solutions allow discussing the transient behaviour
102 of such flow, which has not been studied in the past. Finally, we show that the solutions can
103 be extended to other cases, such as a well intersecting and pumping a vertical fracture of finite
104 length located near an infinite vertical fault zone (Fig. 1b).

105 The proposed solutions should be useful for examining and modelling drawdown created by a
106 pumping well, or a well intersecting and pumping a vertical fracture, near a vertical fault
107 zone, or another vertical geological discontinuity, such as dykes, veins, buried channels
108 embedded in other materials, or even karst conduits.

109

110 **2. Theoretical method and mathematical model**

111 *2.1. Conceptual model*

112 The problem of interest consists in evaluating drawdown as a function of coordinates x , y and
113 time, caused by a pumping well near an infinite vertical fault (or geological discontinuity)
114 with finite thickness, finite storativity and anisotropic hydraulic conductivity (Fig. 1a).
115 Following Anderson's (2006) nomenclature, the system is divided in three domains, D1, D*
116 and D2, with L1 representing the boundary between D1 and D*, and L2 the one between D*
117 and D2. Domain D*, the infinite vertical fault, separates two semi-infinite half-spaces. The
118 pumping well is located in D1; it is at the origin of a Cartesian coordinate system ($x=0$, $y=0$)
119 and is at a distance a from L1. The y -axis is parallel to the two boundaries L1 and L2. The
120 well fully penetrates the aquifer and produces at a constant flowrate Q . The overall domain
121 (D1, D*, D2) assumes a confined condition; each domain is characterized by its own
122 transmissivity and storativity. D* has anisotropic hydraulic conductivity in the horizontal
123 plane, while the two other domains are isotropic. Domain thicknesses can be different (not
124 shown on Fig. 1a). Damage zones along the fault zones (D*) are not considered.

125

126 *2.2. Method of images*

127 The method of images is a classic technique for tackling boundary-value problems, such as
128 those encountered in heat conduction, electrostatics, and, particularly, in groundwater flow, to
129 solve the problem of no-flow, constant boundaries, or leaky boundaries (Ferris et al., 1962;
130 Kruseman et al., 1990; Bruggeman, 1999; Anderson, 2000, 2006). Solutions with this method
131 have the advantage of providing convenient forms, compared to solutions from differential
132 equations that may require numerical inversion of a Laplace transform. The proposed
133 solutions are based upon an unconventional application of the well-image theory. This
134 method, originally proposed by Fenske (1984) for the case of a boundary separating two
135 aquifers with dissimilar diffusivities, and later extended by Dewandel et al. (2014) to a well
136 located in an infinite linear strip aquifer limited on both sides by aquifers of differing
137 properties, has been further developed for the case presented here. Though good and useful
138 approximations, the proposed solutions are not shown to be exact solutions to the appropriate
139 partial differential equations (Bixel et al., 1963; Butler and Liu, 1991; Appendix A, hereafter).
140 We do believe, however, that—although it is not the method used here—drawdown solutions
141 can also be obtained by numerical inversion of a Laplace transform.

142 In a general manner and using the well-image theory for the case presented here, one can
143 consider the drawdown in domain D1 to consist of two components: direct drawdown caused
144 by the pumping well, and reflected drawdowns caused by the reflection of image-well
145 drawdowns from the two boundaries onto D1. Total drawdown can be represented by a sum
146 of drawdowns caused by the pumping well and that caused by image-wells located across the
147 boundaries; each image-well is strengthened to consider the contrast in properties between the
148 three domains. Figure 2a shows the solution for drawdown in D1, where each dot corresponds
149 to an image well with its distance from the pumping well and its strength. This technique is
150 widely used for solving the particular cases of no-flow and constant-head boundary conditions
151 (e.g. Ferris et al., 1962; Kruseman et al., 1990); in these cases, image strength is 1 or -1. More
152 information on the well-image theory can be found in Anderson (2000, 2006), or in
153 Bruggeman (1999).

154 The drawdown in domains D* and D2 is the transmitted drawdown across the boundaries. Its
155 solutions depend upon the properties of the domain of interest and are analogues of the
156 solution in D1. Consequently, drawdown can also be represented as the sum of drawdowns
157 caused by the producing well, and one or two infinite well-image series—depending upon the

158 domain—lying outside the domain of interest, whereby each pumping- and image well was
159 strengthened to cover the aquifer properties of each domain (Figs. 2b and 2c).

160 Along the boundaries, conditions vary from boundary L1 (between D1 and D*) to boundary
161 L2 (between D* and D2) and the following criteria must be satisfied:

162 1). Drawdown must be equal on both sides of the boundaries:

163 - then $s_1(a, y, t) = s^*(a, y, t)$ along boundary L1,

164 - and $s_2(a + h, y, t) = s^*(a + h, y, t)$ along boundary L2,

165 2). Unit discharge orthogonal to the boundaries must be equal on both sides as well:

166 - then $T_1 \frac{\partial s_1(a, y, t)}{\partial x} = T^* \frac{\partial s^*(a, y, t)}{\partial x}$ along boundary L1,

167 - and $T_2 \frac{\partial s_2(a+h, y, t)}{\partial x} = T^* \frac{\partial s^*(a+h, y, t)}{\partial x}$ along boundary L2,

168 where $s_1(x, y, t)$, $s^*(x, y, t)$ and $s_2(x, y, t)$ are the drawdowns in each domain (D1, D* and D2), T_1 ,
169 T^* and T_2 are the transmissivity values of each domain, a is the distance from the pumping
170 well to boundary L1, and h is the width of domain D*.

171

172 2.3. General solutions for drawdown

173 Here, we first considered the case where domain D* is isotropic. A second section deals with
174 the anisotropy of this domain. All three domains are characterized by dissimilar diffusivity
175 values ($T_1/S_1 \neq T^*/S^* \neq T_2/S_2$).

176 Using the well-image theory described above, the general solutions for drawdown valid for
177 each domain are expressed as series (Fig. 2). For domain 1 (D1), drawdown is expressed by
178 that of the producing well, that of one image-well at the opposite of L1 (at $x=2a$), and that of
179 one infinite image-well series lying outside D1. For domain D*, drawdown is expressed by
180 two infinite image-well series lying outside D*, and for D2 by one infinite image-well series
181 lying outside D2.

182 The general form of solutions for drawdown are as follows, for an observation well in domain
183 D1:

$$s_1(x, y, t) = \frac{Q}{4\pi T_1} \left\{ W\left(\frac{S_1}{4T_1 t}(x^2 + y^2)\right) + \alpha_0 W\left(\frac{S_1}{4T_1 t}([2a - x]^2 + y^2)\right) + \sum_{n=2,4,6}^{\infty} \alpha_n W\left(\frac{S_1}{4T_1 t}([2a + nh - x]^2 + y^2)\right) \right\}$$

184

185

(1)

186 For domain D*:

$$s^*(x, y, t) = \frac{Q}{4\pi T^*} \left\{ \sum_{n=2,4,6}^{\infty} \beta'_n W\left(\frac{S^*}{4T^* t}([2a + nh - x]^2 + y^2)\right) + \sum_{n=0,2,4}^{\infty} \beta_n W\left(\frac{S^*}{4T^* t}([2nh + x]^2 + y^2)\right) \right\}$$

187

(2)

188 And for domain D2:

$$s_2(x, y, t) = \frac{Q}{4\pi T_2} \left\{ \sum_{n=0,2,4}^{\infty} \delta_n W\left(\frac{S_2}{4T_2 t}([2nh + x]^2 + y^2)\right) \right\}$$

189

190

(3)

191 where $W(u)$ is the well-function (or exponential integral function also noted $-Ei[-u]$); S_1 and
 192 T_1 (m^2/s) are the storage coefficient and transmissivity of the aquifer in D1, respectively; S^*
 193 and T^* (m^2/s) are those of the strip aquifer in D*, and S_2 and T_2 (m^2/s) those of aquifer D2;
 194 a (m) is the distance from the pumping well to L1; and Q is the pumping rate (m^3s^{-1}); α_0 , α_n ,
 195 β'_i , β_i and δ_i are the image-well strengths. Now, we must evaluate the strength coefficients of
 196 each image-well.

197

198 2.4. Drawdown solutions for the three domains

199 2.4.1. Isotropic case

200 We consider the first series of images according to L1 and L2 (Fig. 3a). The pumping well is
 201 first imaged according to L1. The result of applying the two boundary conditions at boundary

202 L1 ($s_1(a, y, t) = s^*(a, y, t)$ and $T_1 \frac{\partial s_1(a, y, t)}{\partial x} = T^* \frac{\partial s^*(a, y, t)}{\partial x}$) is that the two strength coefficients α_0
 203 and β_0 depend upon the contrast of diffusivity between domains D1 and D*, the distance to
 204 the boundary (a) and time (t). Appendix B gives the detail of their solutions. This case refers
 205 to the influence of a partial hydrologic barrier that separates two domains with contrasted
 206 diffusivities, where the drawdown solutions for both domains D1 and D* correspond to the
 207 ones proposed by Fenske (1984). Then, considering the case of two parallel boundaries L1
 208 and L2, and thus that of a well pumping near an infinite strip aquifer, the pumping well must
 209 be imaged about the second boundary L2 (2nd image), which allows evaluating strength
 210 coefficients β_0' and δ_0 (Fig. 3a), while applying the new boundary conditions ($s_2(a + h, y, t) =$
 211 $s^*(a + h, y, t)$ and $T_2 \frac{\partial s_2(a+h, y, t)}{\partial x} = T^* \frac{\partial s^*(a+h, y, t)}{\partial x}$).

212 These strengths depend upon previous ones β_0 for β_0' , but also on the diffusivity contrast
 213 between domains D* and D2, on the width of domain D* (h), and on time (t); Appendix B
 214 gives the detail of their solutions. Then, as this last image-well does not respect the conditions
 215 at boundary L1, it must be imaged about L1 (3rd image), which allows evaluating strength
 216 coefficients α_1 and β_1 according to boundary conditions in L1 (Fig. 3b). As the 3rd image does
 217 not respect the condition along L2, it has to be imaged about L2 (4th image) and strength
 218 coefficients β_1' and δ_1 should be evaluated according to boundary conditions in L2 (Fig. 3b),
 219 and so on. Therefore, each iteration results in a new image-well with a strength evaluated
 220 according to boundary conditions at L1 and L2. As the strength of the nth image-well depends
 221 upon the product of all previous image-strengths, the strengths of each image-well series can
 222 be expressed as a combination of arithmetic and geometrical series. The drawdown for an
 223 observation well located in D1 is:

$$s_1(x, y, t) = \frac{Q}{4\pi T_1} \left\{ W\left(\frac{S_1}{4T_1 t}(x^2 + y^2)\right) + \frac{T_1 \tau_0 - T^* \gamma_0}{T_1 \tau_0 + T^* \gamma_0} W\left(\frac{S_1}{4T_1 t}([2a - x]^2 + y^2)\right) \right. \\ \left. + \frac{2T^* \gamma_0 \tau_0}{T_1 \tau_0 + T^* \gamma_0} \sum_{n=2,4,6}^{\infty} \frac{2T_1}{T_1 \tau_n + T^* \gamma_n} \prod_{i=1,3,5}^{n-1} \frac{T^* \tau_i - T_2 \gamma_i}{T^* \tau_i + T_2 \gamma_i} \prod_{i=2,4,6}^{n-2} \frac{T^* \gamma'_i - T_1 \tau'_i}{T^* \gamma'_i + T_1 \tau'_i} \right\} \\ W\left(\frac{S_1}{4T_1 t}([2a + nh - x]^2 + y^2)\right) \quad (4)$$

224
 225 with the second geometrical series (the one up to 'n-2') valid for $n > 2$.

226 For a well located in D*, the drawdown is:

$$s^*(x, y, t) = \frac{Q}{4\pi T^*} \left(\frac{2T^* \gamma_0 \tau_0}{T_1 \tau_0 + T^* \gamma_0} \right) \left\{ \sum_{n=2,4,6}^{\infty} \prod_{i=1,3,5}^{n-1} \frac{T^* \tau_i - T_2 \gamma_i}{T^* \tau_i + T_2 \gamma_i} \prod_{i=2,4,6}^{n-2} \frac{T^* \gamma'_i - T_1 \tau'_i}{T^* \gamma'_i + T_1 \tau'_i} \right. \\ \left. + \sum_{n=0,2,4}^{\infty} \prod_{i=1,3,5}^{n-1} \frac{T^* \tau_i - T_2 \gamma_i}{T^* \tau_i + T_2 \gamma_i} \prod_{i=2,4,6}^n \frac{T^* \gamma'_i - T_1 \tau'_i}{T^* \gamma'_i + T_1 \tau'_i} \right\} W \left(\frac{s^*}{4T^* t} ([2a + nh - x]^2 + y^2) \right) \\ W \left(\frac{s^*}{4T^* t} ([nh + x]^2 + y^2) \right) \quad (5)$$

227
228 with the second geometrical series of the first arithmetic series (the one up to ‘n-2’) valid for
229 n>2, and both geometrical series of the second arithmetic series (the ones up to ‘n-1’ and ‘n’)
230 valid for n>1.

231 For a well located in D2, the drawdown is:

$$s_2(x, y, t) = \frac{Q}{4\pi T_2} \left(\frac{2T^* \gamma_0 \tau_0}{T_1 \tau_0 + T^* \gamma_0} \right) \left\{ \sum_{n=0,2,4}^{\infty} \frac{2T_2 \gamma_{n+1} \tau_{n+1}}{T_2 \tau_{n+1} + T^* \gamma_{n+1}} \prod_{i=1,3,5}^{n-1} \frac{T^* \tau_i - T_2 \gamma_i}{T^* \tau_i + T_2 \gamma_i} \prod_{i=2,4,6}^n \frac{T^* \gamma'_i - T_1 \tau'_i}{T^* \gamma'_i + T_1 \tau'_i} \right\} \\ W \left(\frac{S_2}{4T_2 t} ([nh + x]^2 + y^2) \right) \quad (6)$$

232
233 with both geometrical series (the ones up to ‘n-1’ and ‘n’) valid for n>1.

$$234 \text{ with : } \gamma_0 = \frac{W \left(\frac{S_1}{4T_1 t} (a^2 + y^2) \right)}{W \left(\frac{s^*}{4T^* t} (a^2 + y^2) \right)} ; \tau_0 = \frac{e \left(-\frac{S_1}{4T_1 t} (a^2 + y^2) \right)}{e \left(-\frac{s^*}{4T^* t} (a^2 + y^2) \right)}$$

$$235 \gamma_i = \frac{W \left(\frac{s^*}{4T^* t} ([a+ih]^2 + y^2) \right)}{W \left(\frac{S_2}{4T_2 t} ([a+ih]^2 + y^2) \right)} ; \tau_i = \frac{e \left(-\frac{s^*}{4T^* t} ([a+ih]^2 + y^2) \right)}{e \left(-\frac{S_2}{4T_2 t} ([a+ih]^2 + y^2) \right)}$$

$$236 \gamma'_i = \frac{W \left(\frac{S_1}{4T_1 t} ([a+ih]^2 + y^2) \right)}{W \left(\frac{s^*}{4T^* t} ([a+ih]^2 + y^2) \right)} ; \tau'_i = \frac{e \left(-\frac{S_1}{4T_1 t} ([a+ih]^2 + y^2) \right)}{e \left(-\frac{s^*}{4T^* t} ([a+ih]^2 + y^2) \right)}$$

$$237 \gamma_n = \frac{W \left(\frac{S_1}{4T_1 t} ([a+nh]^2 + y^2) \right)}{W \left(\frac{s^*}{4T^* t} ([a+nh]^2 + y^2) \right)} ; \tau_n = \frac{e \left(-\frac{S_1}{4T_1 t} ([a+nh]^2 + y^2) \right)}{e \left(-\frac{s^*}{4T^* t} ([a+nh]^2 + y^2) \right)}$$

$$238 \quad \gamma_{n+1} = \frac{W\left(\frac{S^*}{4T^*t}([a+(n+1)h]^2+y^2)\right)}{W\left(\frac{S_2}{4T_2t}([a+(n+1)h]^2+y^2)\right)}; \tau_{n+1} = \frac{e\left(-\frac{S^*}{4T^*t}([a+(n+1)h]^2+y^2)\right)}{e\left(-\frac{S_2}{4T_2t}([a+(n+1)h]^2+y^2)\right)}$$

239 where $W(u)$ is the exponential integral and $e(u)$ is the exponential function.

240 As a result, the strength coefficients depend upon geometrical series that are a function of
 241 each domain diffusivity, time, the distance a from the pumping well to the first boundary
 242 (L1), and the width h of the strip aquifer (width of D^*). In each infinite series, the strength
 243 coefficient of each image well decreases with distance from both boundaries, and each series
 244 converges absolutely. To solve Eqs. 4 to 6, we used an algorithm based on an iterative
 245 process, where the number of images is determined when the absolute value of a certain
 246 metric given by the n^{th} computation (of the n^{th} becomes negligible (e.g. 10^{-6}). This criterion
 247 ensures high computation accuracy.

248 Note that for the case of time-constant strength coefficients (equal-diffusivity ratio between
 249 the compartments), the solutions are the same as those of the appropriate partial differential
 250 equation. Solutions of this particular case are given in Appendix (C) for the three-aquifer
 251 domains, and, as expected, strength coefficients are identical to the ones given in Anderson
 252 (2006), for a solution in steady-state condition.

253

254 2.4.2. Anisotropic case

255 Analytical solutions for the three domains can be obtained for the case where the geologic
 256 discontinuity (D^*) has an anisotropic transmissivity (or hydraulic conductivity). These
 257 solutions are based on the isotropic solutions (Eqs. 4 to 6) and standard transformed
 258 coordinate techniques (e.g., Hantush, 1966; Ramey, 1975; Neuman et al., 1984). It is assumed
 259 that the main axes of transmissivity in D^* are oriented along the x - and y -directions, thus T_y^*
 260 and T_x^* are parallel and orthogonal to both boundaries, respectively, and $T^* = \sqrt{T_x^*T_y^*}$. As the
 261 pumping well fully penetrates the aquifer (in D1), flow lines are parallel to the bottom of the
 262 aquifer. Consequently, the anisotropy of hydraulic conductivity in the vertical plane is not
 263 considered.

264 According to Bear and Dagan (1965) and Anderson (2006), the transformed coordinates in D1
 265 remain unchanged. However, in D2, x coordinate must be shifted to the right along the x -axis

266 to account for the transformed width of D^* , i.e. $h\sqrt{\frac{T_y^*}{T_x^*}}$. Therefore:

267 in D1, $\dot{x} = x$ and $\dot{y} = y$ (7)

268 and in D2, $\ddot{x} = x + h \left(\sqrt{\frac{T_y^*}{T_x^*}} - 1 \right)$ and $\ddot{y} = y$ (8)

269 In D*, the transformed coordinates are more complex because of rotational flow in D*. They
 270 are $\ddot{x} = x' \sqrt{\frac{T_y^*}{T_x^*}}$ and $\dot{y} = y$, where x' is a function of the real-coordinate system that assumes at
 271 boundary L1 (i.e. between D1 and D*): $\dot{x} = \ddot{x} = x' = a$, and at the second boundary L2 (i.e.
 272 between D* and D2): $\ddot{x} = \ddot{x} = x' = a + h \sqrt{\frac{T_y^*}{T_x^*}}$. These re-scaling relationships show that D*
 273 must also be shifted to the right along the x -axis to account for the transformed width $h \sqrt{\frac{T_y^*}{T_x^*}}$.
 274 According to Dewandel et al. (2014), x' can be estimated empirically; it is found that $x' =$
 275 $x + a \left(\sqrt{\frac{T_x^*}{T_y^*}} - 1 \right)$, which gives for $a \leq x \leq a+h$:

276
$$\ddot{x} = \sqrt{\frac{T_y^*}{T_x^*}}(x - a) + a$$
 (9)

277 The evaluated relationship still depends on the anisotropy ratio in D* and is linear, which
 278 agrees with Baer and Dagan (1965).

279 Drawdown solutions in the transform domains are not re-written as they use isotropic
 280 solutions (Eqs. 4, 5, 6), where h is replaced by $h \sqrt{\frac{T_y^*}{T_x^*}}$ and T^* by $\sqrt{T_x^* T_y^*}$. In Eq. 5 (for an
 281 observation well in D*) x is replaced by \ddot{x} , and in Eq. 6 (for a well in D2) x is replaced by \ddot{x} ,
 282 according to the previous re-scaling rules (Eqs. 9 and 10). The y coordinates remain
 283 unchanged, as well as the x coordinates in Eq. 4 (for a well in domain D1). Re-scaling of all
 284 three domains also satisfies long pumping stages, when drawdown solutions are characterized
 285 by straight lines on semi-log plots whose slope values depend on the average transmissivity of
 286 domains D1 and D2. These solutions are compared with numerical modelling, particularly the
 287 one in D*, in Section 4. *Comparisons between the developed solutions and numerical*
 288 *simulations).*

289

290 **3. Drawdown and flow behaviour at the pumping well**

291 *3.1. Isotropic case*

292 As many type curves exist for describing flow behaviour near such a discontinuity (domain
293 D^*), some examples are given below to discuss the main flow behaviour characteristics.

294 Figure 4 shows the result of Eq. 4 at a pumping well of radius r_w ($x_w = y_w = \sqrt{2}r_w$) using
295 dimensionless time, $t_{DL} = T_1 t / (S_1 a^2)$, and dimensionless drawdown, $s_D(r_w/a, t_{DL}) =$
296 $\frac{2\pi T_1}{Q} s_{pw}(r_w, t)$, for the case where $T_1/S_1=0.1$, $T_2/S_2=0.5$, $T_1/T_2=20.0$, $h=5$ m. Figure 4a presents
297 the case where T^*/T_1 varies from 10^{-2} to 10^3 with $S^*/S_1=20.0$, and Figure 4b the case where
298 S^*/S_1 varies from 10^{-3} to 10^3 with $T^*/T_1=100.0$. Diffusivity in D^* thus varies between 10^{-2} and
299 10^3 . The dimensionless forms of the solutions (Eqs. 4 to 6) are provided as Supporting
300 Information.

301 A convenient starting point for the analysis of Eq. 4 is the log-log diagnostic plot developed
302 by Bourdet et al. (1983). In this plot, both drawdown (s_D) and its derivative (s_D') are shown
303 with respect to the natural logarithm of time ($\partial s_D / \partial \ln(t_{DL})$). Among others, this log-log plot
304 is commonly used for identifying flow regimes during a pumping test (Ehlig-Economides,
305 1988; Bourdet et al., 1989; Spang and Wurstner, 1993; Renard et al., 2009; Ferroud et al.,
306 2019). For all presented derivative curves in this work, derivatives were computed
307 numerically according to Bourdet's et al. (1989) algorithm.

308 During the early stages of pumping, when the cone of depression has not yet reached
309 boundary L1 ($t_{DL} < 0.2$ on Figs. 4a and b), Eq. 4 is identical to the solution of an infinite
310 homogeneous aquifer (Theis, 1935). For a large enough t_{DL} , the condition for which Theis'
311 equation reduces to Cooper-Jacob's (1946) equation, a straight line on a semi-logarithmic plot
312 with a slope $1/2$ characterizes dimensionless drawdown. Its logarithmic derivative is constant
313 (value of $1/2$), reflecting the first infinite-radial flow to the well (Fig. 4). Therefore, for short
314 times, the logarithmic derivative of drawdown will converge to $\partial s / \partial \ln(t) = Q / 4\pi T_1$.

315 Once the cone of depression begins to reach boundary L1 ($t_{DL} > 0.2$), transmissivity and
316 storage-coefficient ratios between the pumped ($D1$) and the strip (D^*) aquifers change the
317 character of the drawdown curves. At that time, the drawdown propagates along boundary L1
318 and within the strip aquifer. For high T^*/T_1 or S^*/S_1 ratios, the derivative slope tends to -1,
319 showing that the fault zone acts as a steady-state source (i.e. constant head boundary;
320 Abbaszadeh and Cinco-Ley, 1995, Abbaszadeh et al., 2000). The higher the T^*/T_1 or S^*/S_1
321 ratios, the more the -1 slope is established and the longer it lasts. Note that this trend generally
322 characterizes a fault zone with infinite hydraulic conductivity near a pumping well

323 (Abbaszadeh and Cinco-Ley, 1995, Abbaszadeh et al., 2000; Escobar et al., 2013). However,
 324 Fig. 4b also shows that a similar trend can be obtained for high S^*/S_I ratios and not
 325 necessarily high T^*/T_I ratios, as in the previously cited literature. Then, at medium-stages
 326 ($t_{DL} > 10.0$), when the fault begins to drain the whole aquifer system, derivatives follow a near
 327 $1/4$ slope, which describes a bi-linear flow regime within D^* , as mentioned in previously cited
 328 work. However, when S^*/S_I ratios are high (> 100.0 on Fig. 4b) the derivative's slope tends to
 329 $1/2$, describing a linear flow regime within D^* . It is also interesting to note that, for
 330 intermediate T^*/T_I ratios (with $T^* > T_I$) or S^*/S_I ratios, drawdown behaves similarly to
 331 naturally fractured media like dual-porosity aquifers (Abbaszadeh and Cinco-Ley, 1995), or
 332 dual-permeability media such as multilayer aquifers.

333 When T^*/T_I and S^*/S_I ratios decrease (Figs. 4a and b), derivative curves rise up, and
 334 durations of the -1 derivative slope period and subsequent $1/4$ or $1/2$ slope decrease (linear flow
 335 regimes), showing that D^* is less able to drain the whole aquifer system. In the proposed
 336 examples, the derivative may form a hump at the end of the linear flow period within D^*
 337 ($t_{DL} > 30$ on Fig. 4a or $6\ 000$ on Fig. 4b). On Fig. 4a, it is the consequence of a decrease in the
 338 T^*/T_I ratio (< 1), and on Fig. 4b it is the result of a lower diffusivity contrast between domains
 339 D^* and D_2 . The smaller the contrast, the greater the hump, which may cause boundary L1
 340 (Fig. 4a) and L2 (Fig. 4b) to appear temporarily as a no-flow boundary (see blue curves on
 341 Fig. 4a).

342 At late pumping stages ($t_{DL} > 10^5$ on Figs. 4a and 4b), drawdown has diffused through the
 343 whole domain D^* and propagates significantly in the third domain (D_2). This period is
 344 characterized by a second radial flow regime, illustrating the overall response of the aquifer
 345 system.

346 During very late stages of pumping (i.e. $t \rightarrow \infty$ or $t_{DL} \rightarrow \infty$), all strength coefficients γ_i and τ_i in
 347 Eq.4, but also in Eqs. 5 and 6, tend to 1. Therefore, and after rearranging Eq. 4, the
 348 logarithmic derivative of the dimensionless drawdown for late-pumping stages leads to:

$$349 \quad \lim_{t_{DL} \rightarrow \infty} \frac{\partial s_D}{\partial t_{DL}} \approx \left(\frac{2T_1}{T_1 + T^*} \right) \left\{ 1 + \left(\frac{2T^*}{T_1 + T^*} \right) \left(\frac{T^* - T_2}{T_2 + T^*} \right) \sum_{n=0,1,2}^{\infty} \left(\frac{T^* - T_2}{T_2 + T^*} \right)^n \left(\frac{T^* - T_1}{T_1 + T^*} \right)^n \right\}$$

350 (10)

351 As $\left(\frac{T^* - T_2}{T_2 + T^*} \right)$ and $\left(\frac{T^* - T_1}{T_1 + T^*} \right)$ ratios are between -1 and 1 , the series can be regarded as a Taylor
 352 series that tends, for $n \rightarrow \infty$, to $\frac{(T_1 + T^*)(T_2 + T^*)}{2T^*(T_1 + T_2)}$. Therefore, the last equation simplifies to

353 $\text{Lim}_{t_{DL} \rightarrow \infty} \frac{\partial s_D}{\partial t_{DL}} \approx \left(\frac{2T_1}{T_1 + T_2} \right)$, showing that the logarithmic derivative of the dimensionless
 354 drawdown depends only on the transmissivities of the pumped aquifer (D1) and of domain
 355 D2. Thus, the logarithmic derivative of drawdown, $\partial s / \partial \ln(t)$, will converge to a constant
 356 value inversely proportional to the average transmissivities of D1 and D2, $\frac{\partial s}{\partial \ln(t)} =$
 357 $Q / [2\pi(T_1 + T_2)]$. This shows that, for late-stage pumping, the drawdown slope does not
 358 depend on the transmissivity of the strip aquifer (D*, representing a fault, another geological
 359 discontinuity, or another compartment), but on those of the pumped compartment and of the
 360 compartment on the other side of the geological discontinuity. This behaviour agrees with
 361 previous work (Abbaszadeh and Cinco-Ley, 1995, Abbaszadeh et al., 2000; Rahman et al.,
 362 2003; Escobar et al., 2013).

363

364 3.2. Anisotropic case

365 As discussed above, the solution with an anisotropic central compartment (D*) is similar to
 366 that for the isotropic case (Eq. 4, h being replaced by $h \sqrt{\frac{T_y^*}{T_x^*}}$ and T^* by $\sqrt{T_x^* T_y^*}$). Therefore,
 367 drawdown and derivative curves are characterized by a similar behaviour (Fig. 5). During the
 368 early-stage pumping ($t_{DL} < 0.2$), $\partial s_D / \partial \ln(t_{DL}) = 1/2$ (or $\partial s / \partial \ln(t) = Q / 4\pi T_1$)—or the first
 369 infinite-acting radial flow when boundary L1 has not been reached by the pumping—and for
 370 late-stage pumping, $\partial s_D / \partial \ln(t_{DL})$ always tends to $\frac{2T_1}{T_1 + T_2}$ (or $\frac{\partial s}{\partial \ln(t)} = Q / [2\pi(T_1 + T_2)]$), which
 371 characterizes the overall response of the aquifer system. However, compared to the isotropic
 372 case ($T_x^* = T_y^*$, curves $T^*/T_I = 100.0$ on Fig. 4a or $S^*/S_I = 20.0$ on Fig. 4b), the T_y^*/T_x^* ratio
 373 increase induces a decrease of the derivative slope, up to -1 for the highest ratios
 374 ($T_y^*/T_x^* > 100.0$), because of the increasing transmissivity contrast (T_y^*/T_I) in a direction
 375 perpendicular to the central compartment (x -axis). This shows that the anisotropy increase of
 376 transmissivity in D*, increases the capacity of the central compartment to drain the entire
 377 system, and thus its capacity to supply water to the pumped D1 compartment. Consequently,
 378 at medium-stage bi-linear flow ($1/4$ derivatives slope) or linear flow ($1/2$ derivatives slope),
 379 regimes are shifted in time. The higher the T_y^*/T_x^* ratio, the greater the offset.

380 Conversely, a decrease in the anisotropy ratio ($T_y^*/T_x^* < 1.0$, Fig. 5) induces a lower
 381 transmissivity contrast between D1 and D* (T_y^*/T_I). This reduces both the exchange between
 382 domains and the capacity of D* to drain the whole system. For the lowest contrast

383 $(T_y^*/T_x^* < 10^{-2})$, D^* may act as a semi-permeable boundary, even though the overall
 384 transmissivity value of D^* is still significantly higher than that of $D1$ ($T^*/T_1=100.0$, Fig. 5).

385

386 **4. Comparison between developed solutions and numerical simulations**

387 We compared the performance of solutions with transmissivity anisotropy in D^* with
 388 numerical modelling, to check their accuracy but also to evaluate Eq. 9 required for the
 389 drawdown solutions in D^* . The numerical modelling was developed with the MARTHE_7.4
 390 ©BRGM computer code (Thiéry, 2010, 2015, 2018). MARTHE allows 2D or 3D modelling
 391 of flow and mass transfers in aquifer systems, including climatic and human influences.
 392 Groundwater flow is computed by a 3-D finite volume approach, to solve the hydrodynamic
 393 equation based on Darcy's law and mass conservation. The grid geometry used in the
 394 numerical model is a 40x40 km square grid with a constant-head boundary condition at each
 395 side. In the x, y plane, cell size varies from 1x1 m at the origin (pumping well) up to
 396 500x500 m near the limits of the model. Vertically, the pumped aquifer is a 100-m-thick layer
 397 subdivided into 25 4-m-thick layers. The aquifer is capped by an impermeable layer (no-flow
 398 condition), creating a confined condition for the pumped layer.

399 Several diffusivity ratios between the three domains and widths of the strip aquifer were
 400 prescribed to test the isotropic and the anisotropic solutions at various observation-well
 401 locations, i.e. in the pumped compartment $D1$, the strip aquifer D^* , and in the right-side
 402 compartment $D2$. Figure 6 shows the results of two of these models for testing the anisotropic
 403 solutions. In the model, the pumping well fully penetrates the aquifer and is located at the
 404 centre of the grid ($x=0; y=0$) and at 12 m ($a=12$ m) from a 8-m-wide strip aquifer ($h=8$ m). In
 405 both cases, transmissivity in the pumped compartment $D1$, T_1 , is 10^{-2} m²/s (hydraulic
 406 conductivity $k_1=10^{-4}$ m/s), the storage coefficient S_1 is 2.0×10^{-2} (specific storage $S_{s1}=2 \times 10^{-4}$ m⁻¹)
 407 and the transmissivity and storage coefficient of the right-hand side compartment ($D2$), T_2 ,
 408 is 5×10^{-3} m²/s ($k_2=5 \times 10^{-5}$ m/s) and S_2 is 10^{-3} ($S_{s2}=10^{-5}$ m⁻¹), respectively. Only the properties
 409 of the strip aquifer (D^*) differ, although the T_y^*/T_x^* anisotropy ratio is the same at 10.0. In
 410 Model 1, T^* is 10^{-1} m²/s ($k^*=10^{-3}$ m/s) and S^* is 10^{-1} ($S_{s^*}=10^{-3}$ m⁻¹), and in Model 2, T^* is
 411 3×10^{-3} m²/s ($k^*=3 \times 10^{-5}$ m/s) and S^* is 2×10^{-2} ($S_{s^*}=2 \times 10^{-4}$ m⁻¹). Thus, in Model 1 the strip
 412 aquifer is the most transmissive and capacitive of the whole domain, while it is the least
 413 transmissive and the least capacitive in Model 2. For the simulations, a constant pumping rate

414 of $Q=1.11 \times 10^{-2} \text{ m}^3/\text{s}$ ($40 \text{ m}^3/\text{h}$) was set up for up to 700 days (about 10^6 min). In this context,
 415 the model's boundaries were not reached, and the aquifer remained saturated.

416 Figures 6a and b compare the results of numerical modelling with analytically computed
 417 drawdown values. As shown on the figures, drawdown values and derivatives computed with
 418 the proposed solutions (Eqs. 4 to 6 with the proposed re-scaling rules of Eqs. 7 to 9), for
 419 observation wells in the pumped aquifer (D1; curves A to D on figures), for the ones in the
 420 strip aquifer (D*; curves E and F) and for the ones in the right-side aquifer (D2; curves G and
 421 H), perfectly match the values from numerical modelling. The root mean square error
 422 (RMSE) was calculated for each numerical-analytical comparison of drawdown values (see
 423 inserted tables on Figures 6a and 6b). RMSE values range between 1.4×10^{-3} and 1.7×10^{-2} m,
 424 showing that the proposed analytical solutions agree with the numerical modelling, a good
 425 indication of their accuracy.

426

427 **5. Flow along and through boundaries L1 and L2**

428 As mentioned in earlier studies, flow through and across a fracture plane or geological
 429 discontinuity (domain D*) is complex, and may be locally reversed (Fig. 7), particularly
 430 where the fault-transmissivity is higher than that of other compartments (Abbaszadeh and
 431 Cinco-Ley, 1995, Abbaszadeh et al., 2000; Rahman et al., 2003). The aim of this section is to
 432 propose analytical solutions of such flows, and to highlight their spatial and transient
 433 evolutions under different diffusivity contrasts ($T_1/S_1 \neq T^*/S^* \neq T_2/S_2$). The dimensionless forms
 434 of the following solutions are provided as Supporting Information.

435 *5.1. Analytical solutions for flows through L1 and L2*

436 Analytical solutions for flow through both boundaries can be derived from Eqs. 4 to 6 for an
 437 isotropic central compartment (D*), and with re-scaling rules presented in section 2.4.2. for
 438 the anisotropic case (Eqs. 7 to 9).

439 The solutions for flow are normalized with respect to the pumping flowrate Q , thus
 440 representing the fraction of Q that flows through L1 and L2 ($\frac{\Delta Q_{L1}}{Q}$, $\frac{\Delta Q_{L2}}{Q}$). Along boundary L1
 441 ($x=a$; between D1 and D*), according to Eq. 4 and for the anisotropic case, the solution is:

$$\begin{aligned} \frac{\Delta Q_{L1}(y, t)}{Q} &= \frac{T_1}{Q} \frac{\partial s_1(a, y, t)}{\partial x} \\ &= \frac{T^* \gamma_0}{\pi(T_1 \tau_0 + T^* \gamma_0)} \left\{ \frac{a}{a^2 + y^2} e^{-\frac{S_1}{4T_1 t}(a^2 + y^2)} \right. \\ &\quad \left. - \tau_0 \sum_{n=2,4,6}^{\infty} \frac{2T_1}{T_1 \tau_n + T^* \gamma_n} \prod_{i=1,3,5}^{n-1} \frac{T^* \tau_i - T_2 \gamma_i}{T^* \tau_i + T_2 \gamma_i} \prod_{i=2,4,6}^{n-2} \frac{T^* \gamma'_i - T_1 \tau'_i}{T^* \gamma'_i + T_1 \tau'_i} \right\} \\ &\quad \left(\frac{nh^* + a}{[a + nh^*]^2 + y^2} \right) e^{-\frac{S_1}{4T_1 t}([a + nh^*]^2 + y^2)} \end{aligned} \tag{11}$$

442
443 and for flow along boundary L2 ($x=a+h$; between D* and D2), according to Eq. 6 and for the
444 anisotropic case, the solution is:

$$\begin{aligned} \frac{\Delta Q_{L2}(y, t)}{Q} &= \frac{T_2}{Q} \frac{\partial s_2(a + h, y, t)}{\partial x} \\ &= \frac{T^* \gamma_0 \tau_0}{\pi(T_1 \tau_0 + T^* \gamma_0)} \left\{ \sum_{n=0,2,4}^{\infty} \frac{2T_2 \gamma_{n+1} \tau_{n+1}}{T_2 \tau_{n+1} + T^* \gamma_{n+1}} \prod_{i=1,3,5}^{n-1} \frac{T^* \tau_i - T_2 \gamma_i}{T^* \tau_i + T_2 \gamma_i} \prod_{i=2,4,6}^n \frac{T^* \gamma'_i - T_1 \tau'_i}{T^* \gamma'_i + T_1 \tau'_i} \right\} \\ &\quad \left(\frac{a + h^*(n + 1)}{[a + h^*(n + 1)]^2 + y^2} \right) e^{-\frac{S_2}{4T_2 t}([a + h^*(n + 1)]^2 + y^2)} \end{aligned} \tag{12}$$

445
446 where $h^* = h \sqrt{\frac{T_y^*}{T_x^*}}$, $T^* = \sqrt{T_x^* T_y^*}$, and where coefficients γ and τ are determined from Eqs. 4 to
447 6 (h is replaced by $h \sqrt{\frac{T_y^*}{T_x^*}}$, and T^* by $\sqrt{T_x^* T_y^*}$). Note that Eq. 11 and Eq. 12 can also be obtained
448 from Eq. 5 (domain D*) at the corresponding boundaries.

449
450 *5.2. Flux profile along L1 and L2*

451 Equations 11 and 12 are complex functions whose behaviour was explored through numerical
452 experiments. Figures 8a and b show the flow profile along both boundaries (i.e. along the y -
453 axis, with $y \geq 0$ both solutions being symmetrical about the x -axis) after 21 days of pumping
454 ($t=3 \times 10^4$ min and $Q=1$ m³/h). For this experiment, the pumping well is located at 10.0 m from
455 a 5-m-wide strip aquifer ($a=10.0$ m and $h=5.0$ m). In all cases, the hydraulic properties in D1
456 are identical ($T_l=10^{-3}$ m²/s; $S_l = 5 \times 10^{-3}$). For curves A to F, the properties of D2 are identical

457 to those of D1 ($T_1=T_2$; $S_1=S_2$), D* is isotropic but its properties differ, T^* varies from 2×10^{-4}
 458 to 2×10^{-2} m²/s and S^* from 10^{-3} to 6×10^{-1} , making compartment D* both the most or the least
 459 transmissive, or the most and the least diffusive aquifer. Curve G is similar to C, but D2 is the
 460 least transmissive, and storativity is the least ($T_2=10^{-4}$ m²/s; $S_2=10^{-3}$). Curve H differs from G
 461 only because D* is anisotropic in transmissivity ($T_y^*/T_x^*=50.0$).

462 Analysis of these curves shows that, as mentioned in earlier studies (Abbaszadeh and Cinco-
 463 Ley, 1995, Abbaszadeh et al., 2000; Rahman et al., 2003), the flow through boundary L1 is
 464 mainly from the compartment D* to D1. Locally, however, it can also be reversed (from D1
 465 to D*) when the central compartment D* becomes the most transmissive aquifer (Fig. 8a,
 466 curves A, B, C, G and H). This flow reversal indicates that, at a certain distance along the y-
 467 axis (or from the pumping well) and after a certain duration of pumping, the hydraulic
 468 gradient at the boundary between D1 and D* is reversed. This implies that streamlines are
 469 reversed, because drawdown within the central compartment propagates faster than in the
 470 surrounding compartments. Such behaviour stems from the higher transmissivity in D*, but
 471 not necessarily because of a higher diffusivity (curves: A, B). For curve E, D* is the most
 472 diffusive, but reversed flow is absent. Curve A presents the equal diffusivity ratio case in
 473 which flow reversal occurs. Regarding the storativity (S^*), the higher the value, the greater the
 474 reversed flow (curves: A, B, C). When compartment D2 on the right-side is the least
 475 transmissive (curves G and H), the flow in D* and therefore the reversed flow (D1 to D*)
 476 increase, and an increase in transmissivity anisotropy of D* ($T_y^* > T_x^*$) enhances the flow
 477 reversal (curve H). When D2 is the least transmissive, reversed flow may occur even if $T^* \leq T_1$,
 478 but with $T^* \geq T_2$ (not shown on the figure), the increase in anisotropy of D* ($T_y^* > T_x^*$) will still
 479 increase such flow. Logically, when D* is the least transmissive, no reversed flow will occur
 480 (curves: D, E, F), as well as when T_2 becomes the most transmissive aquifer (not shown on
 481 the figure).

482 Other tests concerned the distance between the pumping well and L1 (a), and the width of the
 483 central compartment (h). They showed that, regarding distance ' a ', the greater the distance,
 484 the greater the influence of pumping on the pumped compartment (D1), and therefore the less
 485 on D* and D2. Therefore, logically, flows along the two discontinuities are reduced as ' a '
 486 increases. An increase in the width of the central compartment (h) induces an increase in the
 487 lateral transmissivity of the central compartment, perpendicular to the x -axis, which facilitates
 488 the propagation of drawdown in this direction, to the detriment of the y -axis. Consequently,

489 drawdown within the aquifer of the central strip aquifer propagates less rapidly, reducing the
490 reversal hydraulic gradient between D1 and D*, and therefore the reversed flow.

491 Flow along boundary L2 (between D* and D2) is less complex as it is always positive, from
492 D2 to D* (Fig. 8b). It increases when D* is the least transmissive compartment (curves: D, E,
493 F), and decreases when D* is the most transmissive or anisotropic (with $T_{y^*} > T_{x^*}$)
494 compartment (curves: A, B, C, H), or when D2 is the least transmissive (curves G and H).
495 Logically, when D2 is the most transmissive compartment, flow increases (not shown on the
496 figure).

497

498 *5.3. Time-variation of flux along L1 and L2*

499 Figures 9a and b show the evolution of flow profiles through both boundaries for case H on
500 Figure 8 (the anisotropic case $T_{y^*}/T_{x^*}=50.0$), at time of pumping $t=1, 7, 30, 200, 500, 3 \times 10^3,$
501 3×10^4 and 10^8 min. Up until 30 min, the flow at boundary L1 is only from compartment D* to
502 D1, as the hydraulic gradient between D1 and D* is always positive. During this period,
503 particularly from about 2 min, when drawdown begins to reach L1, to 30 min, drawdown does
504 not propagate more rapidly in D1 than in D*. From $t=30$ min the flow reversal starts, as the
505 drawdown begins to propagate faster in D*. The location of the point of reversed flow
506 into/from D*, increases slightly with time. At $t=200$ min the reversal point is at about 48.0 m,
507 and then converges to about 58 m ($y=58.0$ m at $t=10^8$ min). Along L2, the flow from D2 to D*
508 increases with time, particularly for the smallest values of y ($0 \leq y \leq 150-200$ m; $t=1, 7$ and
509 30 min). Then, it flattens for longer time values, but total flow increases significantly. In fact,
510 after 200 min, linear to bi-linear flow regimes start to occur in D* (Fig. 10c), which means
511 that D* begins to drain the two surrounding aquifers (D2 and D1).

512 The precise assessment of flow along L1 (Eq. 11; Figs. 7a and 8a) is a challenging task. It
513 requires separation of the two flow components, the one from D* to D1 (positive flow), and
514 the one from D1 to D* (negative or reversed flow). This implies separating the positive and
515 negative values of the calculation of Eq. 11. The flow at each time t can be calculated by
516 integrating Eq. 11 along the y -axis at the appropriate interval. For flow from D* to D1, the
517 solution is:

$$518 \frac{\Delta Q_{L1}(t)}{q} = 2 \int_0^{y_f} \frac{\Delta Q_{L1}}{q} dy \quad (13)$$

519 and the one from D1 to D* (flow reversal), is:

$$520 \quad \frac{\Delta Q_{L1}(t)}{Q} = 2 \int_{y_f}^{\infty} \frac{\Delta Q_{L1}}{Q} dy \quad (14)$$

521 where $\frac{\Delta Q_{L1}}{Q}$ is given by Eq. 11 and y_f is the location of the point of reversed flow into/from
 522 compartment D* onto the y-axis. However, no formal solution of the roots of Eq. 11 was
 523 found, and they were evaluated numerically using the Newton-Raphson method.

524 For flow along L2, entering compartment D* from D2, Eq. 12 has to be integrated along L2 (-
 525 $\infty < y < \infty$), which gives:

$$526 \quad \frac{\Delta Q_{L2}(t)}{Q} = 2 \int_0^{+\infty} \frac{\Delta Q_{L2}}{Q} dy \quad (15)$$

527 where $\frac{\Delta Q_{L2}}{Q}$ is given by Eq. 12.

528 Note that all integrals in Eqs. 13 to 15 are multiplied by two, to account for symmetrical
 529 properties of equations about the x-axis. Net flow from Domain D* is obtained by subtracting
 530 Eq. 13 from both Eqs. 14 and 15.

531 Figure 10a shows the variations of the various flow components over time, for the anisotropic
 532 example given in Fig. 9 ($T_y^*/T_x^*=50.0$) and for the case where the compartment D* is isotropic
 533 ($T_y^*/T_x^*=1.0$; all other parameters remaining unchanged). Figure 10b presents the net flow
 534 from the strip-aquifer D* (net flow=Eq. 13-[Eq. 14+Eq. 15]). Figure 10c shows the
 535 corresponding drawdowns and their derivatives at the pumping well. Flow entering D1 from
 536 D*, or the one entering D* from D1 (flow reversal), increases sharply once drawdown begins
 537 to propagate significantly in D* (-1 or negative slope on derivatives). Then, once the bi-linear
 538 to linear flow regime is established in D* ($t > 100$ min; Fig. 10c), and drawdown propagates in
 539 the right-side compartment (D2), the flow along L1 increases and then slows down, almost
 540 stabilizing over long times when the whole system responds to pumping (second radial flow
 541 regime). The contribution of the strip-aquifer to compartment D1 varies over time (net flow,
 542 Fig. 10b) according to the various flow components. It first increases rapidly due to the
 543 contribution of D* to D1 (positive flow) and then, once the feature begins to drain the system,
 544 it decreases as reversed flow and flow from D2 increase. Logically, an increase of the
 545 anisotropy ratio in D* increases the net contribution of D*.

546

547 **6. Extension of the proposed theory to a well intersecting and pumping a vertical** 548 **fracture of finite length located near an infinite fault**

549 We propose drawdown solutions for the case of a well intersecting and pumping a vertical
 550 fracture of finite length, $2l$, making an angle α with the x -axis (Fig. 1b; Fig. 11) near an
 551 infinite vertical discontinuity. They are based on the drawdown solutions for the three
 552 compartments developed above for the isotropic and anisotropic cases. The pumping well is
 553 located at the centre of the fracture, at a distance a from L1. The fracture fully penetrates the
 554 aquifer, and should not cross domain D^* (i.e. $l\cos\alpha \leq a$). Assuming that the pumping rate Q is
 555 uniformly distributed along the fracture, i.e. the rate of pumping per unit length of the fracture
 556 is $q(x, y) = Q/2l$, according to Dewandel et al. (2018), drawdown solutions can be obtained
 557 by integrating the above solutions along the fracture axis. Solutions for the three domains then
 558 take the following general form:

$$559 \quad s_{frac}(x, y, t) = \int_{-l}^{+l} s(x, y, t) d\vartheta \quad (16)$$

560 where $s(x, y, t)$ corresponds to Eqs. 4, 5 or 6 for the isotropic case, which, combined with
 561 Eqs. 7, 8 or 9 gives the solutions for the anisotropic case (or $T_y^*/T_x^* \neq 1$). Note that for the
 562 particular case where the distance of the pumped fracture to L1 is infinite ($a \rightarrow \infty$; i.e. there is
 563 only one aquifer system, D1), Eq. 16 corresponds exactly to a known analytical solution
 564 (Gringarten et al. (1974), their Eq. 20) for drawdown in a well pumping a vertical fracture
 565 with uniform flux distribution that fully penetrates the aquifer (Dewandel et al., 2018).

566 The integral in Eq.16 can be evaluated numerically with the Gauss-Legendre quadrature, as
 567 done here, or evaluated using a discretized form of Eq. 16 by dividing the fracture into small
 568 elements and placing the appropriate line-source solution at the centre of each segment
 569 (Dewandel et al., 2018, their Eq. 7).

570

571 6.1. Drawdown and flow behaviours at the pumping well

572 Figure 11 presents the result of Eq. 16 for a pumping well of radius r_w intercepting a fracture
 573 parallel to domain D^* (i.e. parallel to the y -axis, $\alpha=90^\circ$). Dimensionless time according to
 574 fracture length, $t_{Df} = T_1 t / (S_1 l^2)$, and dimensionless drawdown,
 575 $s_{Df}(a/l, t_{Df}) = \frac{2\pi T_1}{Q} s_{pwf}(r_w, t)$, are used for presenting the case where $T_I/S_I=0.1$,
 576 $T^*/S^*=T_2/S_2=0.5$, $T_y^*/T_x^*=10.0$, $T^*/T_I=100.0$; $T_I/T_2=20.0$, $h= 5$ m, and a/l ratios varying from 1
 577 to 10. This setting describes the behaviour of a fracture with increasing distance from
 578 boundary L1.

579 At the start of pumping, the flow is linear (half-unit slope of derivative curves) and
 580 corresponds to flow from aquifer D1 to the fracture intersected by the pumping well. For
 581 intermediate pumping stages, the derivative curves may describe the first infinite-acting radial
 582 flow, when both the boundary L1 has not yet been reached by pumping and the fracture is far
 583 enough from L1, $a/l > 4$. For this case, $\partial s_{Df} / \partial \ln(t_{Df}) = 1/2$ or $\partial s_{frac} / \partial \ln(t) = Q / 4\pi T_1$.
 584 Then, once the cone of depression begins to reach boundary L1, the derivative slope
 585 decreases, and may tend to -1 when the half-fracture size is close to the distance between the
 586 centre of the fracture and L1 ($a/l \leq 3$). This shows that D* acts temporarily as a steady-state
 587 source. At times $t_{Df} > 10.0$ derivatives follow a near $1/4$ slope, describing the earlier-mentioned
 588 bi-linear flow regime within domain D*. As for the case of pumping in a well (without
 589 fracture), the derivative slope may also tend to $1/2$ when S^*/S_l ratios are high (linear flow
 590 regime within D*). For late pumping stages ($t_{Df} > 2 \cdot 10^5$ in Fig. 11), the drawdown has diffused
 591 through the whole domain D* and propagates significantly into the right-side aquifer (domain
 592 D2), indicating that D* drains the whole aquifer system. A second radial flow regime is
 593 encountered and characterizes the overall response of the aquifer system, the derivative
 594 always tending to $\frac{2T_1}{T_1+T_2}$ (or $\frac{\partial s_{frac}}{\partial \ln(t)} = Q / [2\pi(T_1 + T_2)]$), as in previous solutions (see section
 595 3., above).

596

597 6.2. Flow along and through boundaries L1 and L2

598 As done previously for pumping in a well (without fracture), flow along and across both
 599 boundaries L1 and L2 can also be computed using the same procedure as described before
 600 (section 5.). Figures 12 and 13 show examples of flow profiles along L1 and L2 at
 601 $t = 3 \times 10^4$ min, and time-variations of fluxes along L1 and L2, respectively, for pumping in a
 602 20-m-long fracture ($2l = 20$ m) either parallel ($\alpha = 90^\circ$), perpendicular ($\alpha = 0^\circ$), or making a 45°
 603 angle with compartment D* ($\alpha = 45^\circ$). In all cases, the aquifer properties in all three
 604 compartments are identical to case H in Fig. 8 ($T_1 = 10^{-3}$ m²/s, $S_l = 5 \times 10^{-3}$, $T^* = 2 \times 10^{-2}$ m²/s,
 605 $S^* = 10^{-2}$, $T^*_y / T^*_x = 50.0$, $T_2 = 10^{-4}$ m²/s, $S_2 = 10^{-3}$, $h = 5$ m, $a = 10$ m, $Q = 1$ m³/h). The results are
 606 also compared to the case where the well that is pumped does not intersect a fracture.

607 For pumping in a fracture, flow profiles along both boundaries L1 and L2 have a similar
 608 shape compared to the case of pumping in a well, and are logically symmetric to the y-axis
 609 when the fracture is symmetric to the y-axis ($\alpha = 0^\circ$ and 90° ; Fig. 12). Compared to pumping
 610 in a well, flow along boundary L1 (Fig. 12a) is higher near the x-axis ($x = 0$) when the fracture

611 is perpendicular to D^* ($\alpha=0^\circ$), and is logically less important when it is parallel to it ($\alpha=90^\circ$).
612 When the fracture makes a secant angle with D^* ($\alpha=45^\circ$), maximum flow shifts to the side
613 where the fracture is closer to boundary L1 (here, to the right). Reversed flow (from D1 to
614 D^*) is similar in all cases, including the pumping well case, as the reversal point is far from
615 the fracture, at about 50 m.

616 Concerning flow along boundary L2 (Fig. 12b), the same remarks apply, except that for the
617 fracture cases flux distribution is characterized by a sharp distribution almost centred along
618 the x -axis (near $x=0$), and is locally higher than that for the well case. This shows that
619 pumping in a fracture concentrates flow in a larger area, and then solicits more compartment
620 D2 near the fracture.

621 When pumping a fracture, time-variations of flow show similar behaviour to that of the
622 pumping well case (Fig. 13a). In particular, flow reversal is almost identical for all cases. The
623 main difference compared to the pumping well case occurs when the fracture makes a secant
624 angle with D^* ($\alpha=0$ and 45°), forcing D^* , but also D2, to react more rapidly, even at early
625 stages during the linear flow caused by pumping in the fracture (Fig. 13c). However, for late
626 pumping stages, the flow from D^* to D1 is less in the cases considering a fracture when
627 compared to the pumping well case. This difference stems from the larger pumped area that
628 facilitates the reaction of D1 near the pumped fracture. Consequently, the net flow from
629 compartment D^* to D1 (Fig. 13b) is less important when pumping is done through a fracture.

630

631 **7. Conclusions**

632 New analytical solutions for drawdown are proposed for a pumping well, and for a well
633 intersecting and pumping a vertical fracture of finite length, near an infinite vertical fault zone
634 or another vertical geological discontinuity (vein, dyke, strip aquifer) with finite width, finite
635 storativity, and finite—and possibly anisotropic—hydraulic conductivity. Consequently, the
636 solutions proposed can relate to a relatively large set of hydrogeological situations. However,
637 the dip of the structure must be close to vertical and long enough (with regard to the pumping
638 duration) to be considered as infinite for a good use of the solutions (see Fig. 1).

639 The solutions are based on an unconventional application of well-image theory, without
640 limitation on the diffusivity contrast between the aquifer compartments, and considering flow
641 transience within the fault. Solutions were developed for the drawdown in three aquifer

642 compartments, the pumped compartment, the one within the fault zone, and the compartment
643 on the other side of the fault. The solutions are good approximations of the corresponding
644 partial differential equations, and comparison with numerical simulations showed high
645 accuracy.

646 Drawdown and flow regimes in the pumping well were analysed in various configurations
647 and, overall, are similar to previous studies, especially when the fault zone is strongly
648 permeable and anisotropic. In the last case and once the cone of depression reaches the fault,
649 the slope of the logarithmic derivative of drawdown in the pumping well tends to -1, showing
650 that the fault temporarily acts as a steady-state source. Later, when the fault begins to drain
651 the whole aquifer system, the derivative follows typical $\frac{1}{4}$ or $\frac{1}{2}$ slopes, depending upon the
652 contrast in aquifer properties that describe bi-linear to linear flow regimes within the fault
653 zone. For the late stages of pumping, the derivative forms a second radial flow regime that
654 depends upon the average transmissivities of the two external aquifer compartments, but not
655 on the fault zone. The first radial flow is established at an early stage, before the cone of
656 depression reaches the fault zone.

657 This application of image-well theory fits the need for other well functions, which should be
658 derivable on x to get mathematical expressions of strength coefficients. Therefore, drawdown
659 solutions were developed for a well intersecting and pumping a vertical fracture of finite
660 length located near the same infinite vertical fault zone. In terms of flow regimes, behaviour
661 was similar to the pumping well case, except for early pumping stages when a first linear-flow
662 regime defines the response of the pumped vertical fracture. We also believe that other
663 solutions can be derived for a partially penetrating well, or a partially penetrating fracture
664 pumped by a well, located near a 3-D anisotropic fault using the Hantush and Hantush leaky-
665 well functions (Hantush, 1964, 1966; Dewandel et al., 2014). A 3-D geometry of the pumped
666 fracture could be considered as well.

667 An interesting point of the proposed solutions is the possibility to derive transient-flow
668 solutions along both sides of the fault zone, and thus net transient flow from the fault itself.
669 Depending on the contrast in aquifer parameters between the three compartments, flow
670 reversal between the fault and the pumped aquifer occurs, as found in previous work, when
671 the fault zone is the most permeable. We show that net flow from the fault into the pumped
672 aquifer increases rapidly during the early pumping stage due to contribution of the fault zone,
673 and then, once the fault begins to drain the system, it decreases as reversed flow and flow
674 from the opposite-side aquifer increase. Logically, an increasing anisotropy of the fault zone

675 increases the net contribution of the fault. When the pumping takes place through a vertical
676 fracture near a fault zone, net flow is less important because the fracture increases the reaction
677 of the pumped compartment, compared to the fault zone and the opposite-side compartment.
678 Furthermore, all results show that the net flow contribution is characterized by strong time-
679 variation that stabilizes by long pumping stages. This may influence the quality of the pumped
680 water, especially when the water quality of the fault zone is different from that where the well
681 is located. Future work should focus on such flow computations in an experimental site, using
682 geochemical data for assessing the origin of water (or fluid) when pumping a well, or one that
683 intersects and pumps a fracture near a vertical geological discontinuity.

684

685 **Acknowledgements**

686 The authors are grateful for a research-sponsorship from BRGM (France) and from the
687 Dem'Eaux Thau Research Project, co-funded by the French Water Agency of Rhône
688 Mediterranean & Corsica (AEMRC), Balaruc-les-Bains city, the Syndicat Mixte du Bassin de
689 Thau (SMBT), Montpellier Méditerranée Métropole, European Funds for Regional
690 Development, the French Ministry for Research, and Occitanie Region (CPER). The authors
691 thank Francisco J. Valdes-Parada (Editor of the journal) and two anonymous reviewers for
692 their useful comments and remarks. The authors are grateful to Dr. H.M. Kluijver for revising
693 the final version of the English text.

694

695 **References**

- 696 Abbaszadeh M.D., Cinco-Ley H., 1995. Pressure transient behavior in a reservoir with a
697 finite-conductivity fault. SPEFE March 1999; Trans., AIME, , 26-32.
- 698 Abbaszadeh M., Asakawa K., Cinco-Ley H., Arihara N., 2000. Interference testing in
699 reservoirs with conductive faults or fractures. SPE Reservoir Eval. & Eng. 3 (5), 426-434.
- 700 Althawad, M.S., 2016. Semi-analytical solution to a fractured well in an asymmetric reservoir
701 with a finite conductivity fault. PhD Thesis in Petroleum Engineering. Heriot-Watt
702 University, Institute of Petroleum Engineering, Edinburgh U-K, May 2016. 189 p.
- 703 Anderson, E.I., 2000. The method of images for leaky boundaries. Wat. Res., 23, 461-474.

- 704 Anderson, E.I., 2006. Analytical solutions for a flow to a well through a fault. *Adv. in Wat.*
705 *Res.*, 29, 1790-1803.
- 706 Bear J. and G. Dagan, 1965. The relationship between solutions of flow problems in isotropic
707 and anisotropic soils. *J. of Hydrology*, 3, 88-96.
- 708 Bense VF, van Balen RT, De Vries JJ, 2003. The impact of faults on the hydrogeological
709 conditions in the Roer Valley Rift System: an overview. *Netherlands J. Geosci*; 82(1):317–20.
- 710 Bixel, H.C., Larkin B.K., van Poolen H.K., 1963. Effect of linear discontinuities on pressure
711 build-up and drawdown behavior. *J. of Petr. Techn*, August 1963, 885-895.
- 712 Bourdet, D., Whittle T.M., Dougals, A.A., Pirard V.M., 1983. A new set of type curves
713 simplifies well test analysis, *World Oil.*, 95-106, Gulf Publishing Co., Houston.
- 714 Bourdet D., Ayoud J.A., Pirard Y.M., 1989. Use of pressure derivative in well-test
715 interpretation. *SPE*, 293-302.
- 716 Boussila, A.K., Taib, D., Owayed, J., 2003. Pressure behavior of well near a leaky boundary
717 in heterogeneous reservoirs. *SPE 80911*, <https://doi.org/10.2118/80911-MS>
- 718 Bruggeman, G.A., 1999. *Analytical Solutions of Geohydrological Problems*. Developments in
719 *Water Science* 46, Elsevier, The Netherlands, 959 p.
- 720 Butler, J.J. Jr., Liu W.Z., 1991. Pumping tests in non-uniform aquifers—The linear strip case.
721 *J. of Hydrol.*, 128, 69-99.
- 722 Caine JC, Evans JP, Forster CB. Fault zone architecture and permeability structure. *Geology*
723 1996;24(11):1025–8.
- 724 Cooper, H.H. and C.E. Jacob, 1946. A generalized graphical method for evaluating formation
725 constants and summarizing well field history, *Am. Geophys. Union Trans.*, vol. 27, pp. 526-
726 534.
- 727 Dewandel, B., Lachassagne, P., Zaidi, F.K., Chandra, S., 2011. A conceptual hydrodynamic
728 model of a geological discontinuity in hard rock aquifers: example of a quartz reef in granitic
729 terrain in South India. *J. of Hydrol.*, 405, 474–487.
- 730 Dewandel, B., Maréchal, J.C., Bour, O., Ladouche, B., Ahmed, S., Chandra, S., Pauwels H.,
731 2012. Upscaling and regionalizing hydraulic conductivity and efficient porosity at watershed
732 scale in crystalline aquifers. *J. of Hydrol.*, 416-417, 83-97.

- 733 Dewandel B., Aunay B., Maréchal J.C., Roques C., Bour O., Mougin B. and L. Aquilina,
734 2014. Analytical solutions for analysing pumping tests in a sub-vertical and anisotropic fault
735 zone draining shallow aquifers. *J. of Hydrology*, 509, 115–131.
- 736 Dewandel B., S. Lanini, P. Lachassagne, J.-C. Maréchal, 2018. A generic analytical solution
737 for modelling pumping tests in wells intersecting fractures. *J. of Hydrology*, 559, 89–99,
738 <https://doi.org/10.1016/j.jhydrol.2018.02.013>.
- 739 Ehlig-Economides, C.A., 1988. Use of the pressure derivative for diagnosing pressure-
740 transient behavior. *J. Petrol. Technol.* (October), 1280–1288.
- 741 Escobar, F. H., Martínez, J. A. & Montealegre-Madero, M., 2013. Pressure transient analysis
742 for a reservoir with a finite-conductivity fault. *CT&F - Ciencia, Tecnología y Futuro*, 5(2), 5-
743 18.
- 744 Fenske, P.R., 1984. Unsteady drawdown in the presence of a linear discontinuity. In:
745 Rosenshein, J., Bennett G.D. (Eds.), *Groundwater Hydraulics*. AGU Water Res. Monogr., 9,
746 125-145.
- 747 Ferris, J.G., Knowles, D.B., Brown, R.H., Stallman R.W., 1962. Theory of aquifer tests.
748 U.S.G.S. Water-Supply Paper. 1536-E, 69-174.
- 749 Ferroud A., Rafini S., Chesnaux R., 2019. Using flow dimension sequences to interpret non-
750 uniform aquifers with constant-rate pumping-tests: A review. *Journ. of Hydrology X*, 1-25.
751 <https://doi.org/10.1016/j.hydroa.2018.100003>
- 752 Gringarten, A.C., Henry, J., Ramey, H.J., Raghavan, R., 1974. Unsteady state pressure
753 distributions created by a well with a single infinite conductivity vertical fracture. *J. Soc. Petr.*
754 *Eng.* 14, 347–360.
- 755 Haneberg, W.C., 1995. Steady state groundwater flow across idealized faults. *Water Resour*
756 *Res.* 31(7):1815–20.
- 757 Hantush, M.S., 1964. Hydraulics of wells. In: Chow, V.T. (Ed.), *Advances in Hydrosience*,
758 vol. 1. Academic Press, New York, NY.
- 759 Hantush, M.S., 1966. Analysis of data from pumping tests in anisotropic aquifers. *J. Geoph.*
760 *Res.* 72, 1709–1720.

- 761 Kruseman, G.P., de Ridder, N.A., Verweij J.M., 1990. Analysis and evaluation of pumping
762 test data. 2nd ed. Wageningen, The Netherlands. ILRI publication 47, 377p.
- 763 Lachassagne P., Wyns, R., Dewandel B., 2011. The fracture permeability of Hard Rock
764 Aquifers is due neither to tectonics, nor to unloading, but to weathering processes. *Terra*
765 *Nova*, 23, 145–161, 2011.
- 766 Lachassagne P., Dewandel B., Wyns R. 2021. Review: Hydrogeology of weathered
767 crystalline/hard-rock aquifers—guidelines for the operational survey and management of their
768 groundwater resources. 1-34. *Hydrog. Journ.* <https://doi.org/10.1007/s10040-021-02339-7>
- 769 Perrin J., Ahmed S., Hunkeler D., 2011. The role of geological heterogeneities and
770 piezometric fluctuations on groundwater flow and chemistry in hard-rock, southern India.
771 *Hydrogeology J.* 19 (6), 1189–1201. <http://dx.doi.org/10.1007/s10040-011-0745-y>.
- 772 Maréchal J.C., Ladouche B., Dewandel B., Fleury P., Dörfliger N., 2014. Diagnostic Plots
773 Applied to Well-Tests in Karst Systems. J. Mudry et al. (eds.), *H2Karst Research in*
774 *Limestone Hydrogeology*, *Envir. Earth Science*, doi:10.1007/978-3-319-06139-9_9.
- 775 Maslia M.L., Prowell D.C., 1990. Effect of faults on fluid flow and chloride contamination in
776 a carbonate aquifer system. *J Hydrol*;115: 1–49.
- 777 Maximov, V.A., 1962. Unsteady flow of compressible fluid to wells in a heterogeneous
778 medium. *Appl. Mech. Tech. Phys.* 3, 109–112 (in Russian).
- 779 Neuman, S.P., Walter, G.R., Bentley, H.W., Ward, J.J., Gonzalez, D.D., 1984. Determination
780 of horizontal aquifer anisotropy with three wells. *Ground Water* 22, 66–72.
- 781 Nind, T.E.W., 1965. Influence of absolute and partial hydrogeologic barriers on pump test
782 results. *Can. J. Earth Sci.* 2, 309–323.
- 783 Rafini, S., Larocque, M., 2009. Insights from numerical modeling on the hydrodynamics of
784 non-radial flow in faulted media. *Adv. Water Resour.* 32, 1170–1179.
785 <https://doi.org/10.1016/j.advwatres.2009.03.009>.
- 786 Rafini, S., Larocque M., 2012. Numerical modeling of the hydraulic signatures of horizontal
787 and inclined faults. *Hydrogeol. J.*, 20, 337–350.
- 788 Raghavan, R., 2004. A review of applications to constrain pumping test responses to improve
789 on geological description and uncertainty. *Rev. of Geoph.*, 42, 1-29.

- 790 Raghavan, R., 2010. A composite system with a planar interface. *J. Petrol. Sci. Eng.* 70, 229–
791 234.
- 792 Ramey, H.J., 1975. Interference analysis for anisotropic formations – a case history. *J. Petr.*
793 *Techn.*, 1290–1298.
- 794 Renard, Ph., Glenz, D., Mejias, M., 2009. Understanding diagnostic plots for well-test
795 interpretation. *Hydrogeol. J.*, 17, 589–600.
- 796 Spane, F.A., Wurstner, S.K., 1993. DERIV: a computer program for calculating pressures
797 derivatives for use in hydraulic test analysis. *Ground Water* 31, 814–822.
- 798 Thiéry, D., 2010. Groundwater flow modelling in porous media using MARTHE. In: Tanguy,
799 J.M. (Ed.), *Modelling Software Volume 5. Environmental Hydraulics Series. Editions*
800 *Wiley/ISTE, London*, pp. 45–60.
- 801 Thiéry, D., 2015. Code de calcul MARTHE - Modélisation 3D des écoulements dans les
802 hydro-systèmes - Notice d'utilisation de la version 7.5, BRGM/RP-64554-FR, Orléans.
- 803 Thiéry D., Amraoui N., Noyer M.-L., 2018. Modelling flow and heat transfer through
804 unsaturated chalk – Validation with experimental data from the ground surface to the aquifer.
805 *J. of Hydrology*, 556, 660–673. <https://doi.org/10.1016/j.jhydrol.2017.11.041>
- 806 Xiong Y., Xiong W., Cai M., Hou C. a, Wang C., 2017. Laboratory experiments of well
807 testing for fracture-cave carbonate gas reservoirs. *Petroleum*, 3, 301-308.
808 <http://dx.doi.org/10.1016/j.petlm.2016.09.004>
- 809 Xu Y., Hu W., Pang W., 2018. A new method for diagnosing caves in fault-karst carbonate
810 reservoirs. *Society of Petroleum Engineers*, SPE-192971-MS. 1-8.
- 811 Yaxley, L.M., 1987. Effect of a partially communicating fault on transient pressure behavior.
812 *S.P.E. paper 14311*, 60th Annual Fall Meeting, Las Vegas, Nv.
- 813

814 **List of symbols:**

815 a : distance to boundary L1 in m

816 e^x : exponential function

817 h : width of domain D* (linear strip aquifer), in m

818 l : half-fracture length (in Domain 1), in m

819 Q : pumping flow rate, in m^3s^{-1}

820 r_w : well radius, in m

821 S_1, S^*, S_2 : storage coefficients of the right-side compartment (D1), the strip aquifer (D*), and
822 the left-side compartment (D2), respectively, dimensionless

823 s_1, s^*, s_2 : drawdown of the right-side compartment (D1), the strip aquifer (D*), and the left-
824 side compartment (D2), respectively, in m

825 s_{frac} : drawdown for a well intersecting and pumping a vertical fracture, in m

826 s_D : dimensionless drawdown for pumping in a well; $s_D(r_w/a, t_{DL}) = \frac{2\pi T_1}{Q} s_{pw}(r_w, t)$

827 s_{Df} : dimensionless drawdown for a well intersecting and pumping a vertical fracture;

828 $s_{Df}(a/l, t_{Df}) = \frac{2\pi T_1}{Q} s_{pwf}(r_w, t)$

829 t_{DL} : dimensionless time according to the distance to the boundary (for pumping in a well);

830 $t_{DL} = T_1 t / (S_1 a^2)$

831 t_{Df} : dimensionless time according to the fracture half-length (for a well intersecting and

832 pumping a vertical fracture); $t_{Df} = T_1 t / (S_1 l^2)$

833 t : time, in seconds

834 T_1, T^*, T_2 : transmissivity of the right-side compartment (D1), the strip aquifer (D*), and the
835 left-side compartment (D2) respectively, in m^2/s

836 T_x^* and T_y^* : principal axes of transmissivity anisotropy in the horizontal plane of the strip
837 aquifer (D*), in m^2/s

838 x, y : coordinates of a Cartesian system, in m

839 $W(u) = \int_u^\infty \frac{e^{-\varepsilon}}{\varepsilon} d\varepsilon$ with ε a variable of integration. Well function.

840 α : angle of the fracture with the x -axis, radian

841

842 **Appendices**843 **Appendix A *Partial differential equation***

844 In D1 (Bixel et al., 1963; Butler and Liu, 1991):

845
$$\frac{\partial^2 s_1}{\partial x^2} + \frac{\partial^2 s_1}{\partial y^2} + \frac{Q}{T_1} \delta(x)\delta(y) = \frac{s_1}{T_1} \frac{\partial s_1}{\partial t}. \quad (\text{A.1})$$

846 $\delta(x)\delta(y)$ is a combination of Dirac delta functions representing the pumping well as a line
847 source at $x=y=0$.

848 In D* (Butler and Liu, 1991):

849
$$\frac{\partial^2 s^*}{\partial x^2} + \frac{\partial^2 s^*}{\partial y^2} = \frac{s^*}{T^*} \frac{\partial s^*}{\partial t} \quad (\text{A.2})$$

850 And in D2 (Butler and Liu, 1991):

851
$$\frac{\partial^2 s_2}{\partial x^2} + \frac{\partial^2 s_2}{\partial y^2} = \frac{s_2}{T_2} \frac{\partial s_2}{\partial t} \quad (\text{A.3})$$

852

853 **Appendix B Calculation of strength coefficients for the first series of image-wells**
854 **according to boundaries L1 and L2 (Fig. 3a)**855 We first consider the first image according to L1 (boundary between D1 and D*; Fig. 3a). In
856 this case, the problem refers to the influence of a partial hydrologic barrier on a well test
857 (Bixel et al., 1963; Fenske, 1984; Maximov, 1962; Nind, 1965; Raghavan, 2010).

858 Applying the first boundary condition, it results that drawdown in Domain 1 is:

859
$$s_1(x, y, t) = \frac{Q}{4\pi T_1} \left[W\left(\frac{s_1}{4T_1 t}(x^2 + y^2)\right) + \alpha_0 W\left(\frac{s_1}{4T_1 t}([2a - x]^2 + y^2)\right) \right] \quad (\text{B.1})$$

860 and that drawdown in Domain D* is:

861
$$s^*(x, y, t) = \frac{Q}{4\pi T^*} \beta_0 W\left(\frac{s^*}{4T^* t}(x^2 + y^2)\right) \quad (\text{B.2})$$

862 Equating Eqs. (B.1) and (B.2), and for the condition $x=a$ (i.e. $s_1(a, y, t) = s^*(a, y, t)$) at the
863 boundary L1, we obtain:

864
$$1 + \alpha_0 = \frac{T_1 \beta_0}{T^* \gamma_0} \quad \text{with } \gamma_0 = \frac{W\left(\frac{s_1}{4T_1 t}(a^2 + y^2)\right)}{W\left(\frac{s^*}{4T^* t}(a^2 + y^2)\right)} \quad (\text{B.3})$$

865 Then, applying the second boundary condition at boundary L1, $T_1 \frac{\partial s_1(a,y,t)}{\partial x} = T^* \frac{\partial s^*(a,y,t)}{\partial x}$, gives:

$$866 \quad 1 - \alpha_0 = \frac{\beta_0}{\tau_0} \text{ with } \tau_0 = \frac{e\left(-\frac{S_1}{4T_1 t}(a^2+y^2)\right)}{e\left(-\frac{S^*}{4T^* t}(a^2+y^2)\right)} \quad (\text{B.4})$$

867 Equating Eqs. (B.3) and (B.4) gives the strength coefficients α_0 and β_0 :

$$868 \quad \alpha_0 = \frac{T_1 \tau_0 - T^* \gamma_0}{T_1 \tau_0 + T^* \gamma_0} \quad \text{and } \beta_0 = \frac{2T^* \tau_0 \gamma_0}{T_1 \tau_0 + T^* \gamma_0} \quad (\text{B.5})$$

869 This case, which considers a system composed of only two domains (D1 and D*), is exactly
870 the solution proposed by Fenske (1984) for various diffusivity contrasts ($T_1/S_1 \neq T^*/S^*$).

871 Now, the pumping well must be imaged about the second boundary L2, and it results that
872 drawdown in Domain D* is:

$$873 \quad s^*(x, y, t) = \frac{Q}{4\pi T^*} \left[\beta_0 W\left(\frac{S^*}{4T^* t}(x^2 + y^2)\right) + \beta'_0 W\left(\frac{S^*}{4T^* t}[(2a - x)^2 + y^2]\right) \right] \quad (\text{B.6})$$

874 and that drawdown in Domain 2 is:

$$875 \quad s_2(x, y, t) = \frac{Q}{4\pi T_2} \delta_0 W\left(\frac{S_2}{4T_2 t}(x^2 + y^2)\right) \quad (\text{B.7})$$

876 Equating Eqs. (B.6) and (B.7), and for the condition $x=a+h$ ($s_2(a+h, y, t) = s^*(a+h, y, t)$) at
877 the boundary L2, we obtain:

$$878 \quad \beta_0 + \beta'_0 = \frac{T^* \delta_0}{T_2 \gamma_1} \text{ with } \gamma_1 = \frac{W\left(\frac{S^*}{4T^* t}[(a+h)^2 + y^2]\right)}{W\left(\frac{S_2}{4T_2 t}[(a+h)^2 + y^2]\right)} \quad (\text{B.8})$$

879 Applying the second boundary condition at boundary L2, $T_2 \frac{\partial s_2(a+h,y,t)}{\partial x} = T^* \frac{\partial s^*(a+h,y,t)}{\partial x}$, gives:

$$880 \quad \beta_0 - \beta'_0 = \frac{\delta_0}{\tau_1} \text{ with } \tau_1 = \frac{e\left(-\frac{S^*}{4T^* t}[(a+h)^2 + y^2]\right)}{e\left(-\frac{S_2}{4T_2 t}[(a+h)^2 + y^2]\right)} \quad (\text{B.9})$$

881 Equating Eqs. (B.8) and (B.8) gives the strength coefficients β'_0 and δ_0 :

$$882 \quad \beta'_0 = -\beta_0 \frac{T_2 \tau_1 - T^* \gamma_1}{T_2 \tau_1 + T^* \gamma_1} \text{ and } \delta_0 = \frac{2T_2 \tau_1 \gamma_1}{T_2 \gamma_1 + T^* \tau_1} \quad (\text{B.10})$$

883

884 Calculation of strength coefficients for the second series of image-wells according to L1 and
885 L2 (Fig. 3b).

886 Drawdown in Domain 1 is:

$$887 \quad s_1(x, y, t) = \frac{Q}{4\pi T_1} \alpha_1 W\left(\frac{S_1}{4T_1 t} ([2a + 2h - x]^2 + y^2)\right) \quad (\text{B.11})$$

888 Drawdown in Domain D* is:

$$889 \quad s^*(x, y, t) = \frac{Q}{4\pi T^*} \left[\beta'_0 W\left(\frac{S^*}{4T^* t} ([2a + 2h - x]^2 + y^2)\right) + \beta_0 W\left(\frac{S^*}{4T^* t} ([2h + x]^2 + y^2)\right) \right] \\ 890 \quad (\text{B.12})$$

891 Drawdown in Domain D2 is:

$$892 \quad s_2(x, y, t) = \frac{Q}{4\pi T_2} \delta_1 W\left(\frac{S_2}{4T_2 t} [(2h + x)^2 + y^2]\right) \quad (\text{B.13})$$

893 Applying the two boundary conditions at each boundary, first at L1 and then at L2, results
894 that strength coefficients α_l , β'_0 , β_l , β'_1 and δ_l are given by:

$$895 \quad \alpha_1 = \beta'_0 \frac{2T_1}{T_1 \tau_2 + T^* \gamma_2}, \beta_1 = \beta'_0 \frac{T^* \gamma_2 - T_1 \tau_2}{T^* \gamma_2 + T_1 \tau_2}, \beta'_1 = -\beta_1 \frac{T_2 \tau_3 - T^* \gamma_3}{T_2 \tau_3 + T^* \gamma_3} \text{ and } \delta_1 = \beta_1 \frac{2T_2 \tau_3 \gamma_3}{T_2 \gamma_3 + T^* \tau_3} \quad (\text{B.14})$$

$$896 \quad \text{with } \gamma_2 = \frac{W\left(\frac{S_1}{4T_1 t} ([a+2h]^2 + y^2)\right)}{W\left(\frac{S^*}{4T^* t} ([a+2h]^2 + y^2)\right)}, \tau_2 = \frac{e\left(-\frac{S_1}{4T_1 t} ([a+2h]^2 + y^2)\right)}{e\left(-\frac{S^*}{4T^* t} ([a+2h]^2 + y^2)\right)}, \gamma_3 = \frac{W\left(\frac{S^*}{4T^* t} [(a+3h)^2 + y^2]\right)}{W\left(\frac{S_2}{4T_2 t} [(a+3h)^2 + y^2]\right)} \text{ and}$$

$$897 \quad \tau_3 = \frac{e\left(-\frac{S^*}{4T^* t} [(a+3h)^2 + y^2]\right)}{e\left(-\frac{S_2}{4T_2 t} [(a+3h)^2 + y^2]\right)}$$

898 and so on.

899

900 **Appendix C Drawdown solutions for the equal diffusivity case ($T_1/S_1=T^*/S^*=T_2/S_2=\eta$)**

901 For Domain 1:

$$902 \quad s_1(x, y, t) = \\ 903 \quad \frac{Q}{4\pi T_1} \left\{ W\left(\frac{x^2 + y^2}{4\eta t}\right) + \frac{T_1 - T^*}{T_1 + T^*} W\left(\frac{[2a - x]^2 + y^2}{4\eta t}\right) + \right. \\ 904 \quad \left. \left(\frac{-2T^*}{T_1 + T^*}\right) \left(\frac{2T_1}{T_1 + T^*}\right) \left(\frac{T_2 - T^*}{T_2 + T^*}\right) \sum_{n=0,1,2}^{\infty} \left(\frac{T_1 - T^*}{T_1 + T^*}\right)^n \left(\frac{T_2 - T^*}{T_2 + T^*}\right)^n W\left(\frac{[2a + 2(n+1)h - x]^2 + y^2}{4\eta t}\right) \right\} \quad (\text{C.1})$$

905 For Domain D*:

$$\begin{aligned}
 906 \quad s^*(x, y, t) &= \frac{Q}{4\pi T^*} \left\{ \left(\frac{-2T^*}{T_1+T^*} \right) \left(\frac{T_2-T^*}{T_2+T^*} \right) \sum_{n=0,1,2}^{\infty} \left(\frac{T_1-T^*}{T_1+T^*} \right)^n \left(\frac{T_2-T^*}{T_2+T^*} \right)^n \text{W} \left(\frac{[2a+2(n+1)h-x]^2+y^2}{4\eta t} \right) + \right. \\
 907 \quad &\left. \left(\frac{2T^*}{T_1+T^*} \right) \sum_{n=0,1,2}^{\infty} \left(\frac{T_1-T^*}{T_1+T^*} \right)^n \left(\frac{T_2-T^*}{T_2+T^*} \right)^n \text{W} \left(\frac{[2nh+x]^2+y^2}{4\eta t} \right) \right\} \quad (C.2)
 \end{aligned}$$

908 And for Domain 2:

$$909 \quad s_2(x, y, t) = \frac{Q}{4\pi T_2} \left(\frac{2T^*}{T_1+T^*} \right) \left(\frac{2T_2}{T_2+T^*} \right) \left\{ \sum_{n=0,1,2}^{\infty} \left(\frac{T_1-T^*}{T_1+T^*} \right)^n \left(\frac{T_2-T^*}{T_2+T^*} \right)^n \text{W} \left(\frac{[nh+x]^2+y^2}{4\eta t} \right) \right\} \quad (C.3)$$

910 Note that for this particular case, strength coefficients are identical to the ones given by
 911 Anderson (2006) for a steady-state solution.

912

913 **Figure captions**

914 Figure 1. Conceptual sketches: a) of a pumping well and b) of a well intersecting and
 915 pumping a vertical fracture with finite length, located near a vertical infinite and anisotropic
 916 fault zone, (or another vertical geological discontinuity, strip aquifer). Domain D^* (width h)
 917 separates two semi-infinite half-spaces of dissimilar properties (domains D_1 and D_2). The
 918 pumping well, or the pumped vertical fracture, is located in D_1 and is not connected to D^* .

919 Figure 2. Graphical display of the image-well series. (a) Image-well according to L1 and L2,
 920 graphical display of the image-well series. (b) Observation well located in domain D_1 .
 921 (c) Observation well located in domain D^* . (d) Observation well located in domain D_2 .
 922 Modified from Anderson (2006). The pumping well is located in D_1 .

923 Figure 3. Graphical display of the first image-wells and calculation of the corresponding
 924 strength coefficients. (a) First series of image-wells according to L1 and L2. (b) Second series
 925 of images according to L1 and L2.

926 Figure 4. Type-curves of dimensionless drawdown (s_D) and derivatives s_D' , and dimensionless
 927 time (t_{DL}) for a pumping well near a vertical infinite and isotropic fault zone (D^*). $T_1/S_1=0.1$,
 928 $T_2/S_2=0.5$, $T_1/T_2=20.0$, $h=5$ m. (a) Variations of transmissivity contrast T^*/T_1 (10^{-2} to 10^3)
 929 with $S^*/S_1=20.0$. (b) Variations of storativity contrast S^*/S_1 (10^{-3} to 10^3) with $T^*/T_1=100.0$.

930 Figure 5. Type-curves of dimensionless drawdown (s_D) and derivatives s_D' , and dimensionless
 931 time (t_{DL}) for a pumping well near a vertical infinite and anisotropic fault zone. Anisotropy
 932 ratio varies ($10^{-3} \leq T_y^*/T_x^* \leq 10^3$) $T_1/S_1=0.1$, $S^*/S_1=20.0$, $T^*/S^*=T_2/S_2=0.5$, $T_1/T_2=20.0$, $h=5$ m.

933 Figure 6. Comparison of drawdown, s , and derivative, s' , computed with MARTHE software
 934 (plain dots: s ; open dots: s') and the analytical solutions (plain curves: s ; dotted curves: s') for
 935 the anisotropic case (Eqs. 4-6 with Eqs. 7-9). See figure and text for model parameters. The
 936 inserted tables show RMSE values for various observation-well locations (x , y coordinates).
 937 (a) Model 1: T^* : 10^{-1} m²/s and S^* : 10^{-1} . (b) Model 2 T^* : 3×10^{-3} m²/s and S^* : 2×10^{-2} . In both
 938 cases, $T_y^*/T_x^*=10.0$. ‘‘

939 Figure 7. Conceptual sketch of flow behaviour through boundaries L1 and L2, where the
 940 transmissivity of the central compartment (D^* , fault zone) is higher than that of other
 941 compartments. Black arrows: normal flow from compartment D^* to D_1 , or D_2 to D^* . Blue
 942 arrows: flow reversal from D_1 to D^* . Pumping is performed in D_1 .

943 Figure 8. Flow profiles through both discontinuities. (a) L1 and (b) L2 with various aquifer
 944 properties after 21 days of pumping ($t=3 \times 10^4$ min and $Q=1$ m³/h). The pumping well is
 945 located at 10.0 m from a 5-m-wide fault zone ($a=10.0$ m and $h=5.0$ m). See figure and text for
 946 model parameters.

947 Figure 9. Flow profiles through both discontinuities. (a) L1 and (b) L2 at various times of
 948 pumping, $t=1, 7, 30, 200, 500, 3 \times 10^3, 3 \times 10^4$ and 10^8 min. It corresponds to case H on Figure 7
 949 (the anisotropic case $T_y^*/T_x^*=50.0$). See figure and text for model parameters.

950 Figure 10. (a) Time-variations of the various flow components through both discontinuities
 951 L1 and L2. (b) Net flow from strip aquifer D*. (c) Corresponding drawdowns and their
 952 derivatives at the pumping well. Two examples are shown, the one given on Figure 8
 953 ($T_y^*/T_x^*=50.0$, case H) and the one where D* is isotropic ($T_y^*/T_x^*=1.0$), all other parameters
 954 remaining unchanged.

955 Figure 11. Type-curves of dimensionless drawdown (s_{Df}) and derivatives s_{Df}' , and
 956 dimensionless time (t_{Df}) for a well intersecting and pumping a vertical fracture near a vertical
 957 infinite and anisotropic strip aquifer (Fig. 1b). Variations of a/l ratios (from 1 to 10),
 958 $T_1/S_1=0.1, T^*/S^*=T_2/S_2=0.5, T_y^*/T_x^*=10.0, T^*/T_1=100.0; T_1/T_2=20.0, h=5$ m.

959 Figure 12. Flow profiles through both boundaries: (a) L1 and (b) L2 for a well intersecting
 960 and pumping a vertical fracture near a vertical infinite fault zone at $t=3 \times 10^4$ min. $T_1=10^{-3}$
 961 m²/s, $S_1=5 \times 10^{-3}, T^*=2 \times 10^{-2}$ m²/s, $S^*=10^{-2}, T_y^*/T_x^*=50.0, T_2=10^{-4}$ m²/s, $S_2=10^{-3}, h=5$ m and
 962 $a=10$ m, $Q=1$ m³/h, fracture length $2l=20$ m, and $\alpha=0^\circ, 45^\circ$ and 90° (a : angle of the fracture
 963 according to the x -axis). We also presented the case where a well is pumped without fracture
 964 (grey curve H on Fig. 8).

965 Figure 13. (a) Time-variations of flux along L1 and L2. (b) Net flow from fault zone D*.
 966 (c) Corresponding drawdown and derivatives at a well intersecting and pumping a fracture.
 967 Aquifer properties are identical to the examples shown on Fig. 12. We also present the case
 968 where a well is pumped, without fracture (in grey, the same as on Fig. 9).

969

970

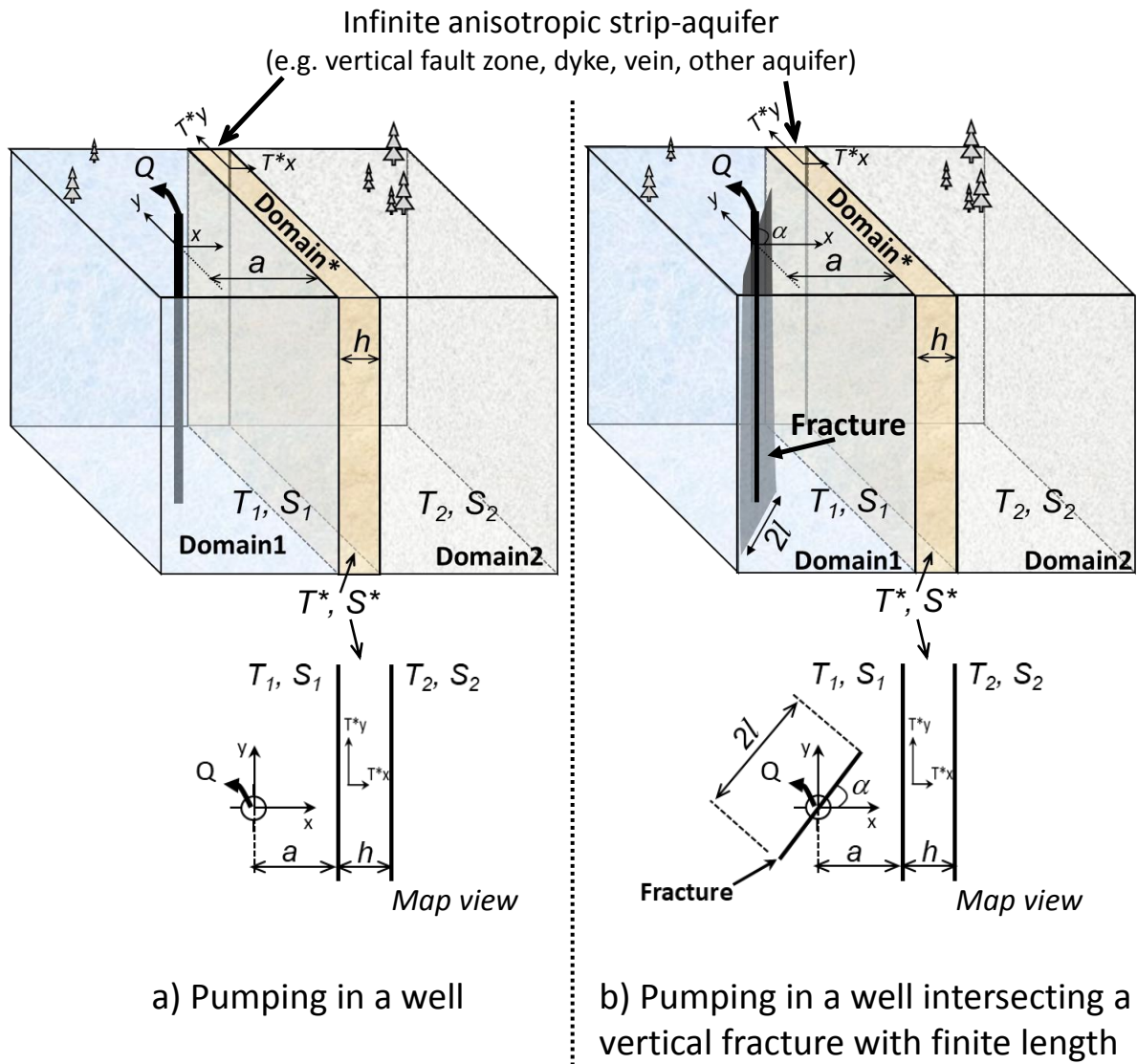
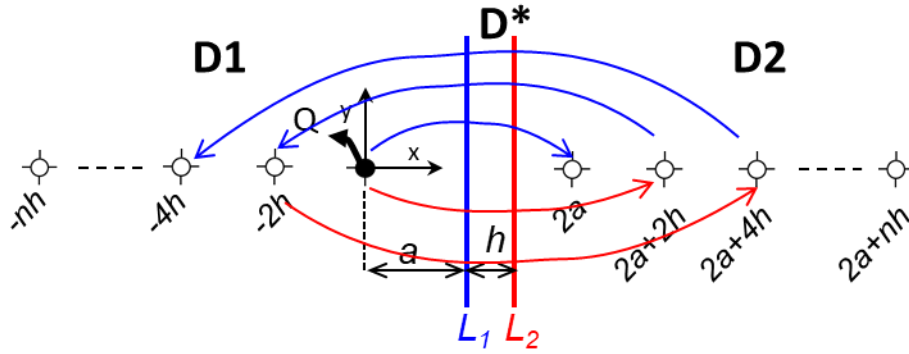
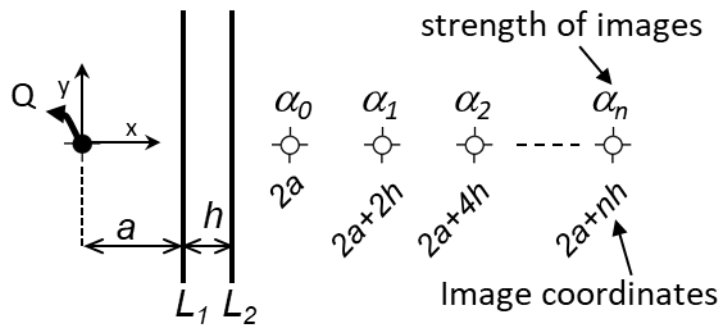


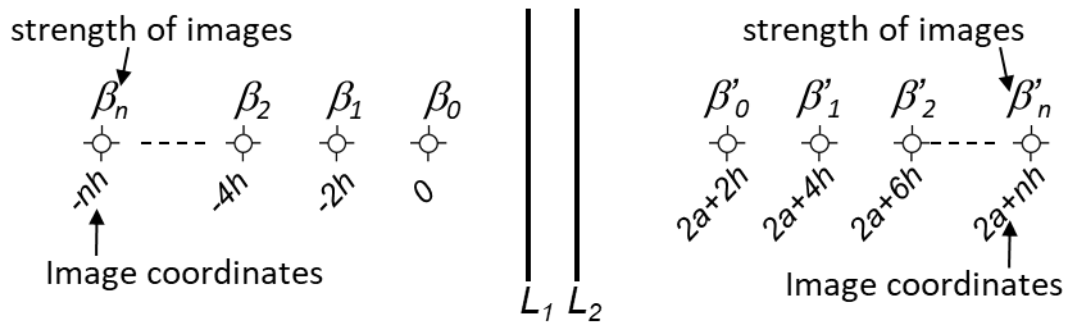
Figure 1



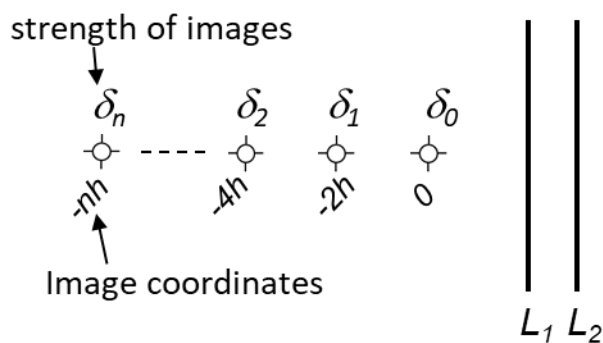
(a) Image-wells according to boundaries L_1 and L_2



(b) For an observation well located in Domain 1

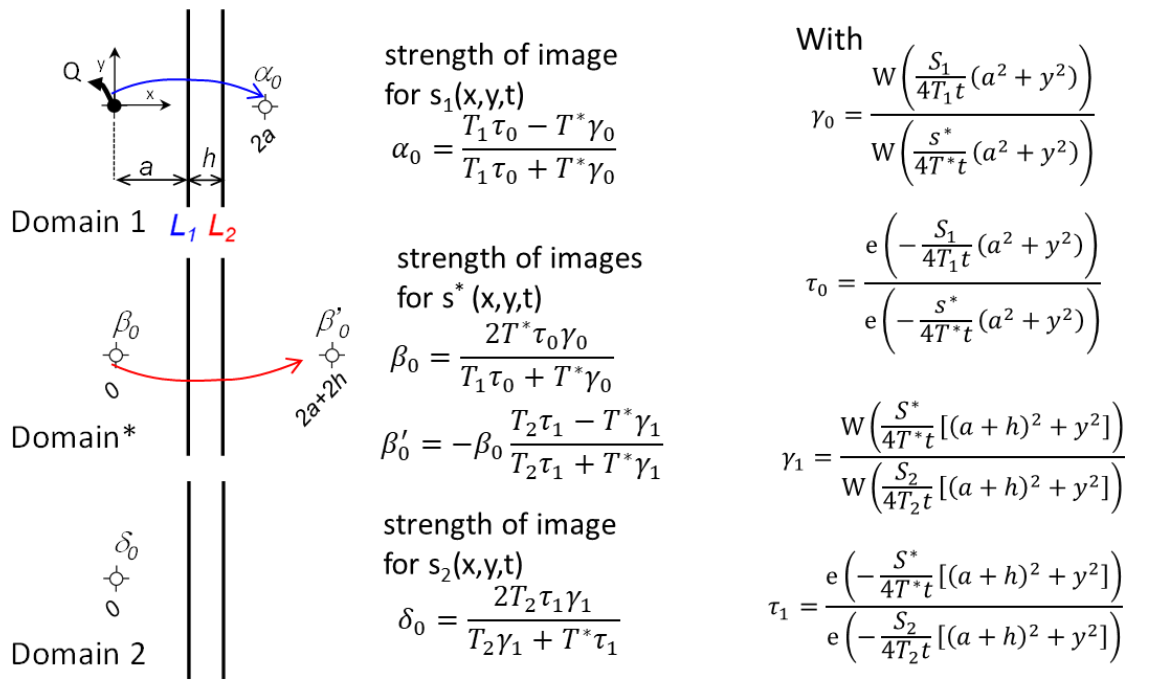


(c) for an observation well located in Domain *

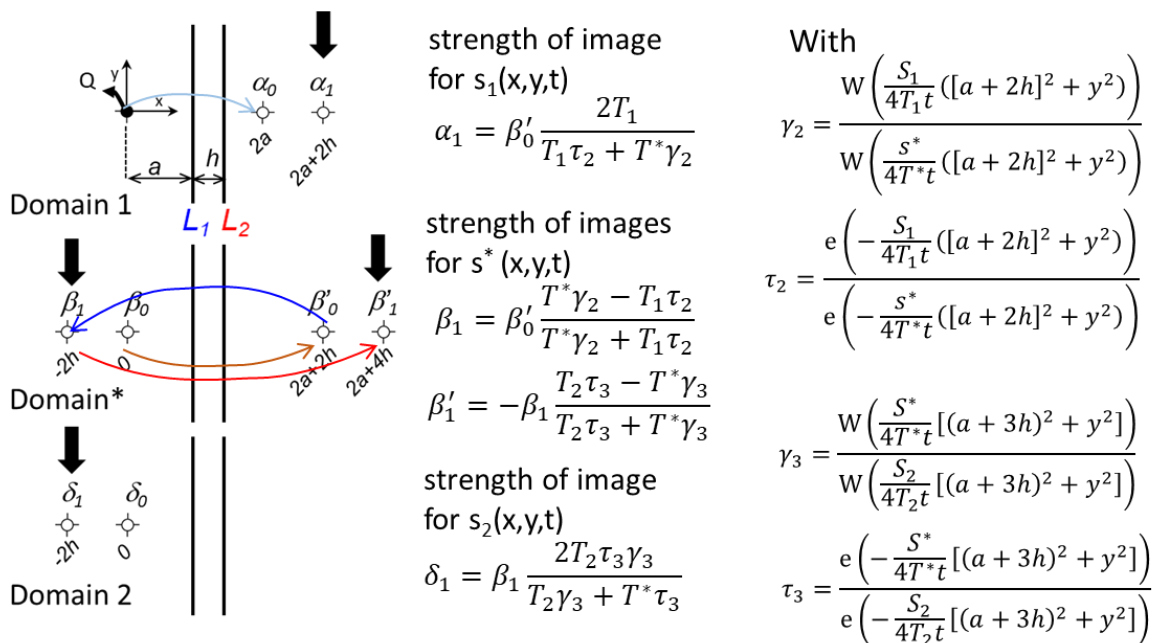


(d) for an observation well located in Domain 2

Figure 2

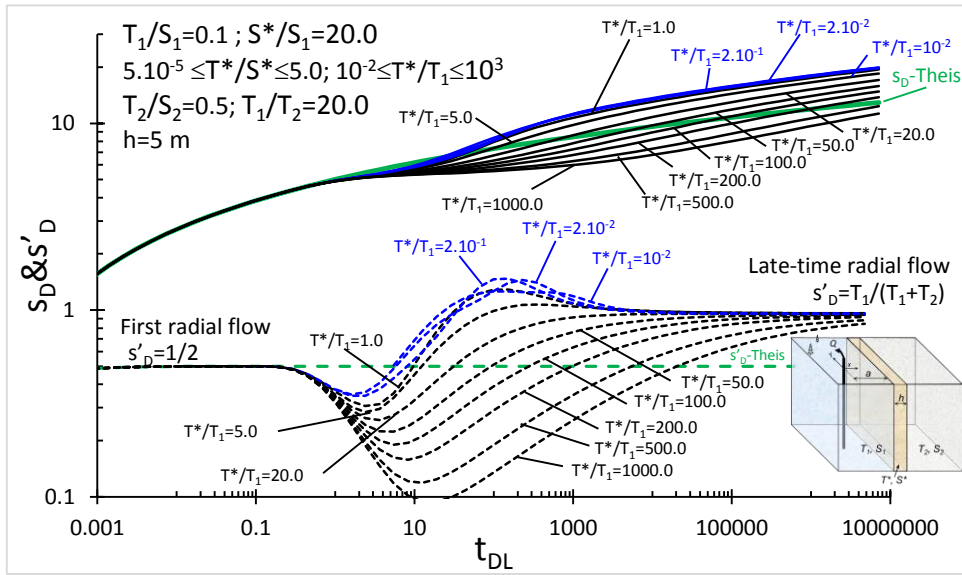


(a) first series of image-well according to L1 and L2

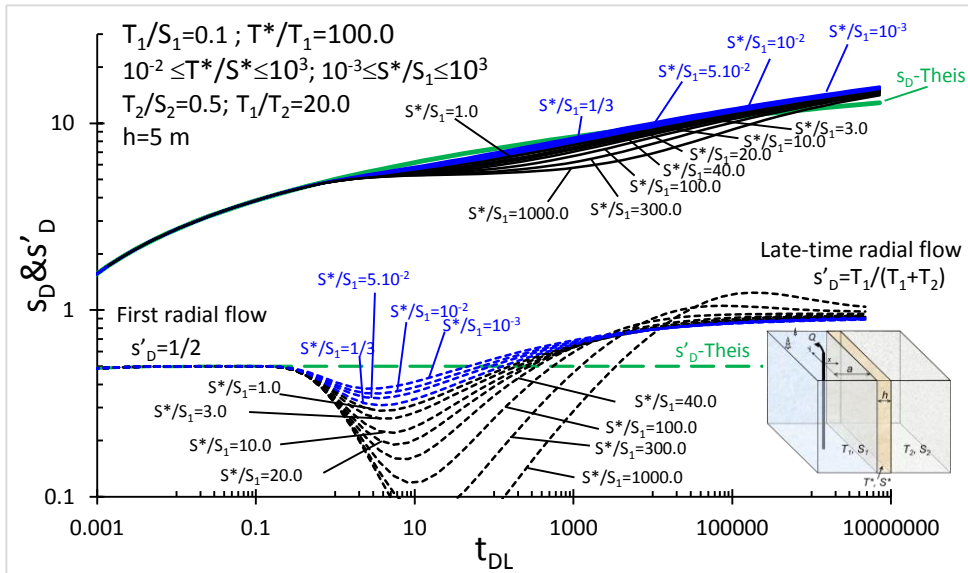


(b) second series of images according to L1 and L2

Figure 3



(a)



(b)

Figure 4

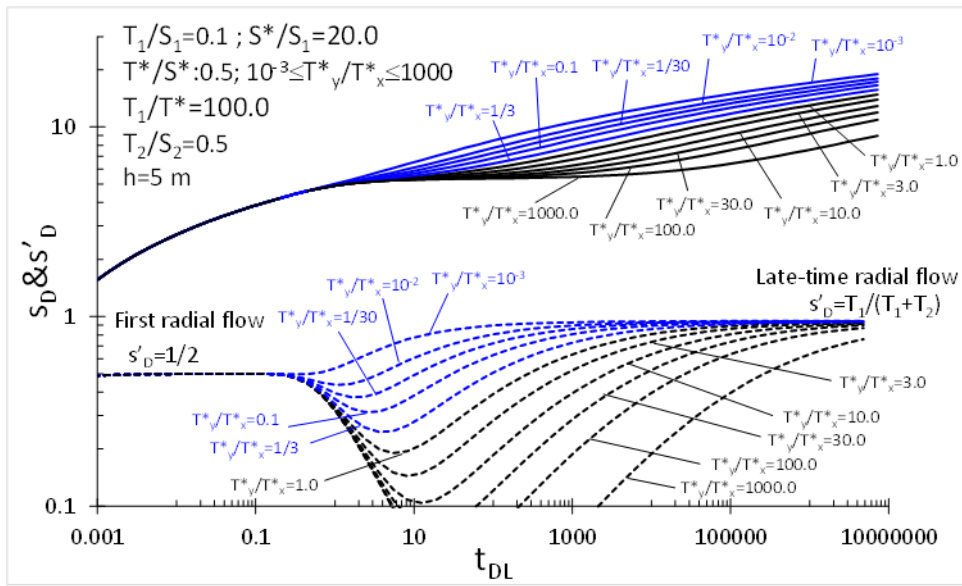


Figure 5

975

976

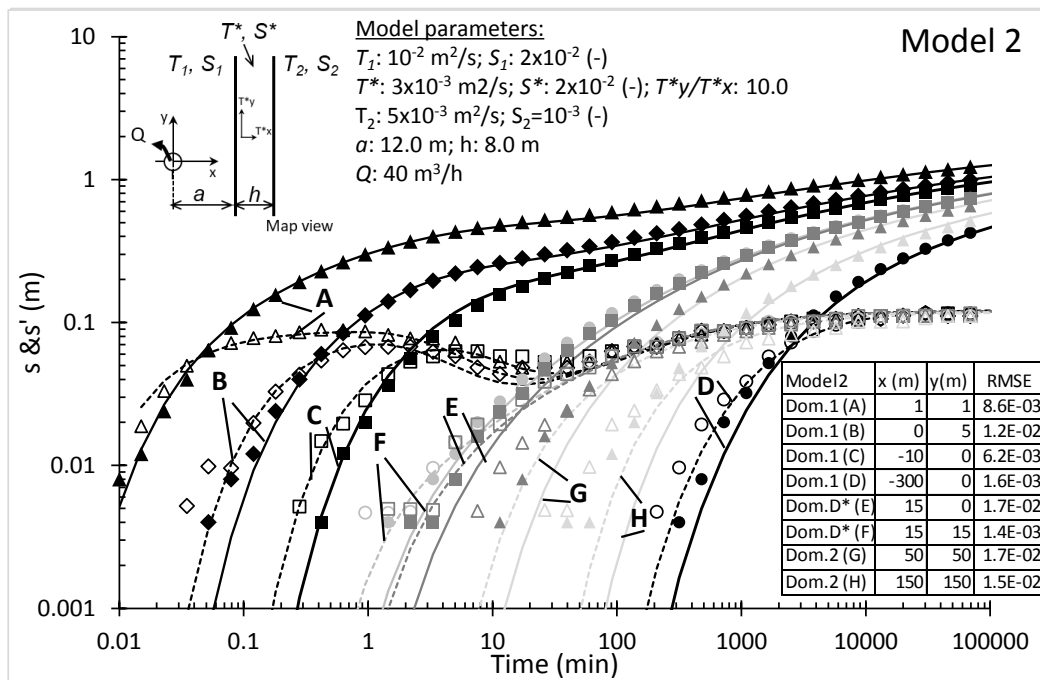
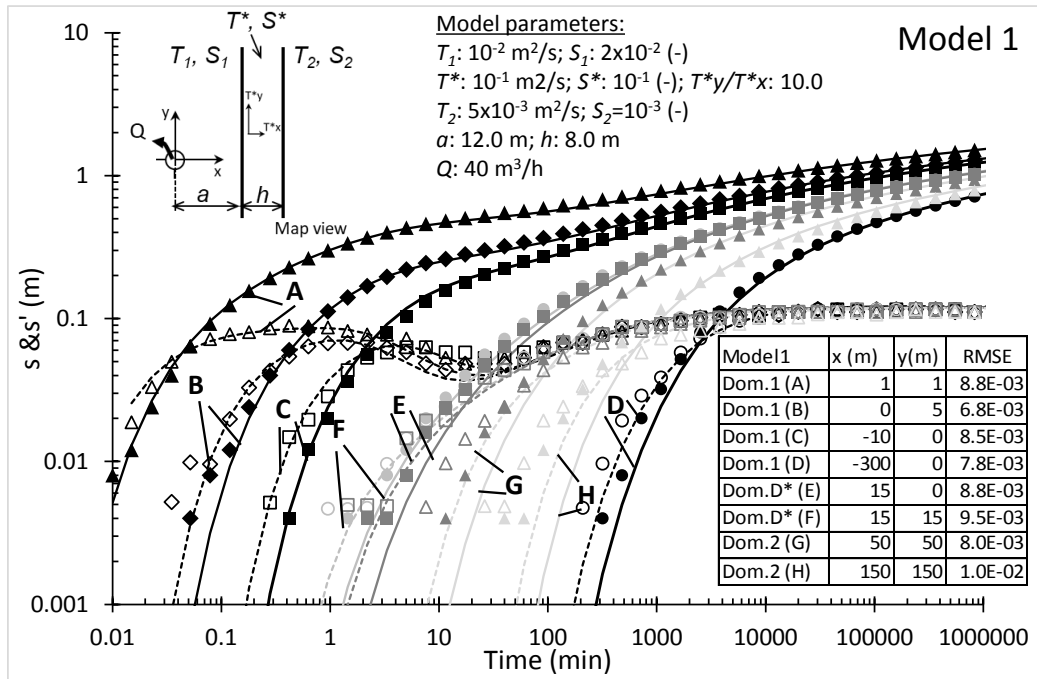


Figure 6

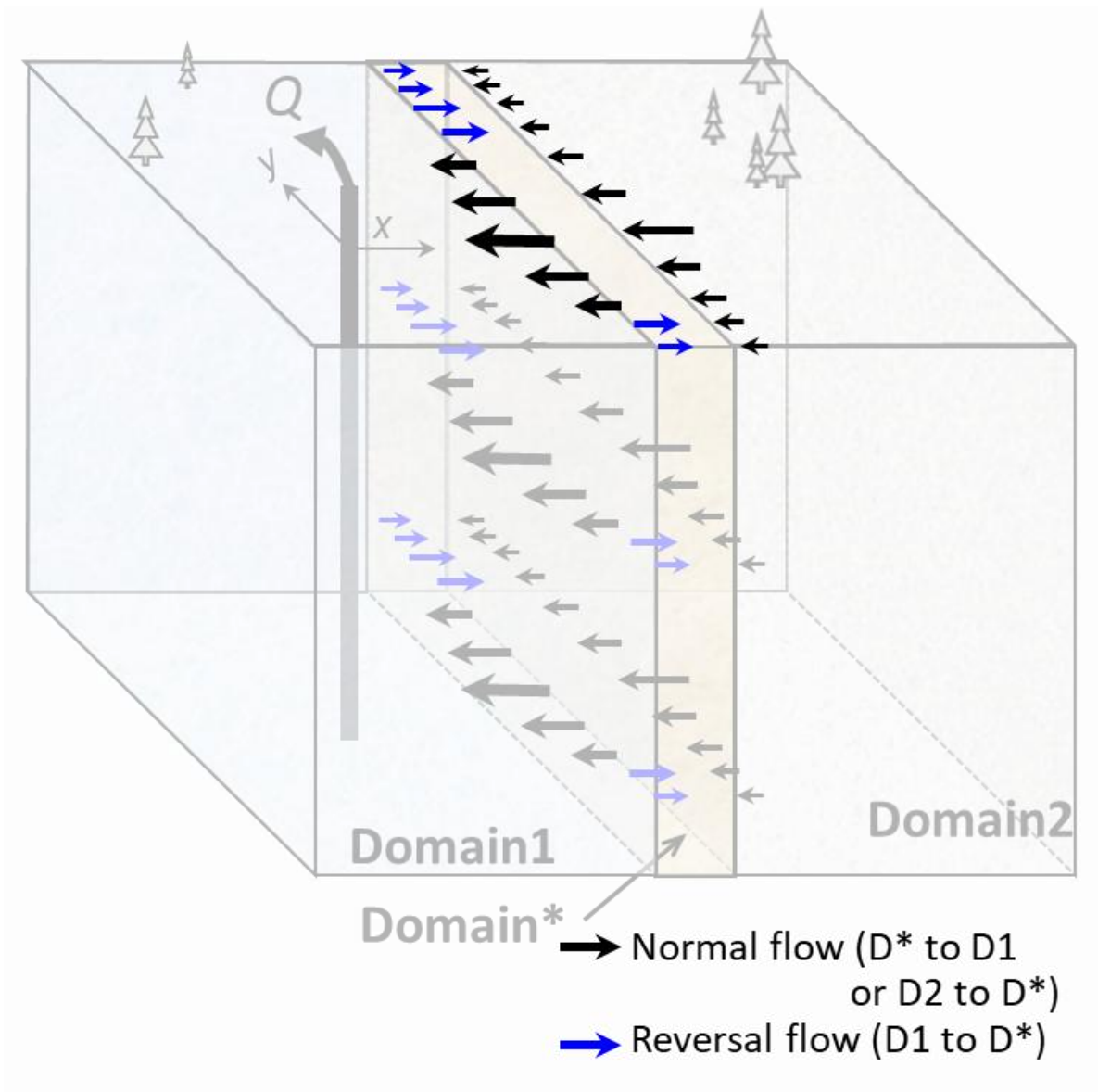


Figure 7

978

979

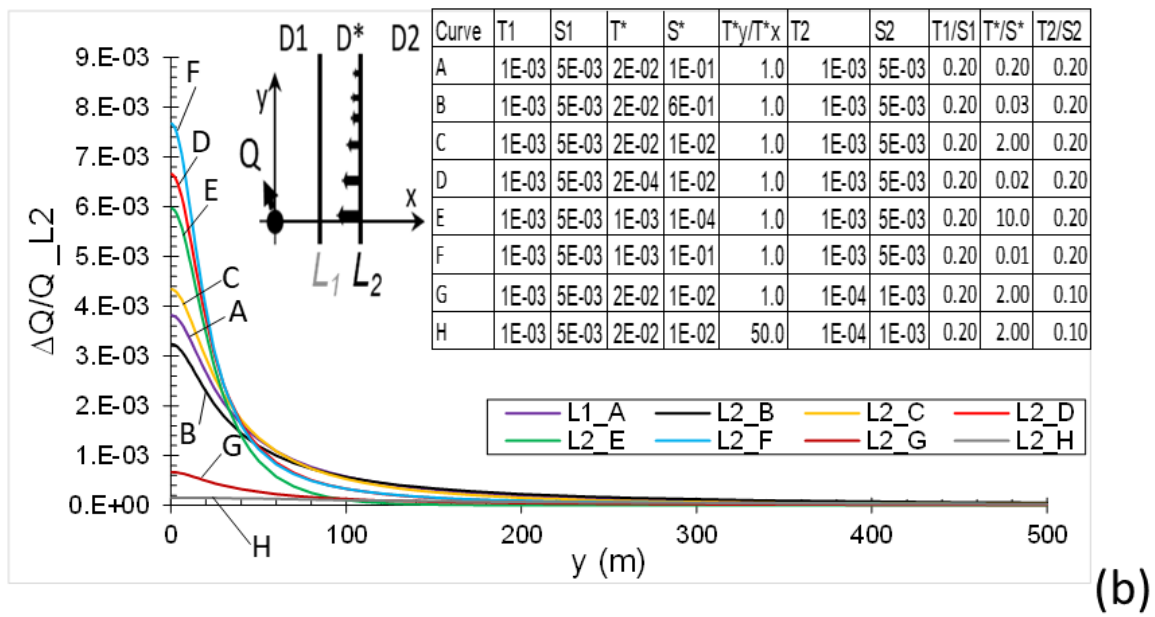
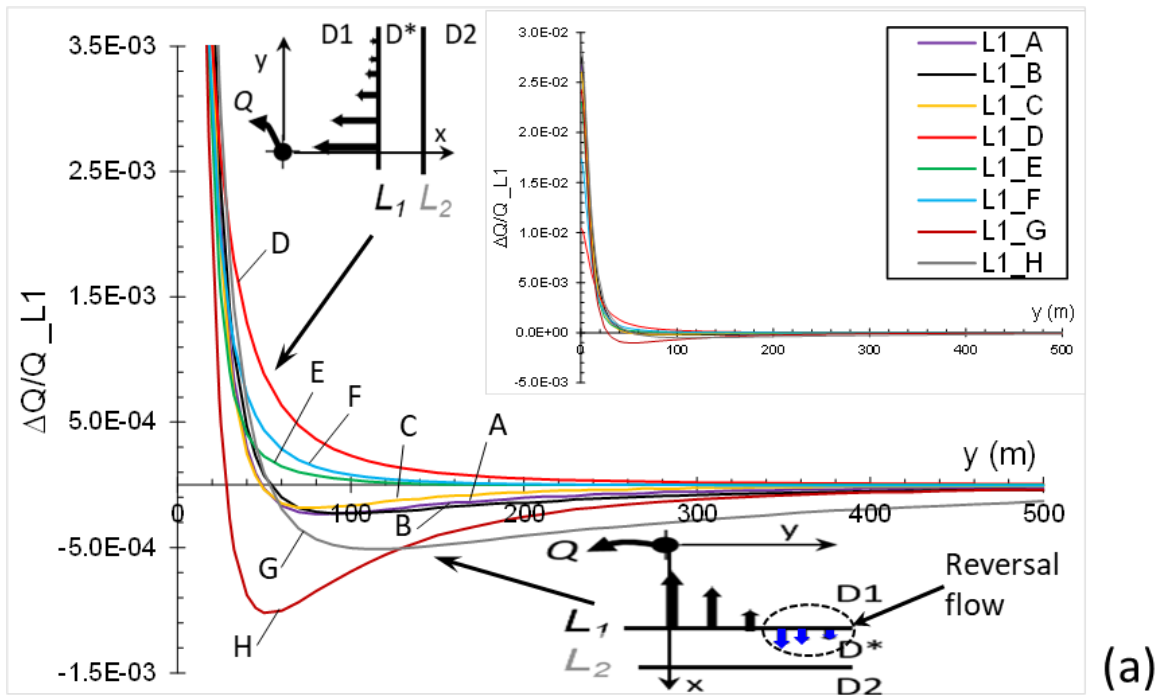


Figure 8

980

981

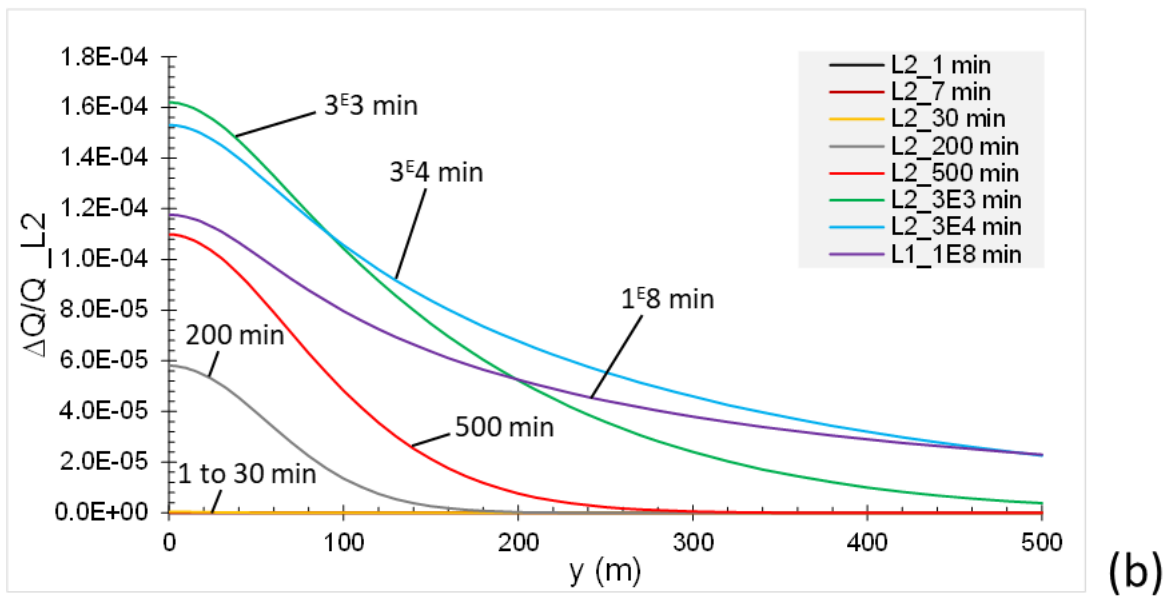
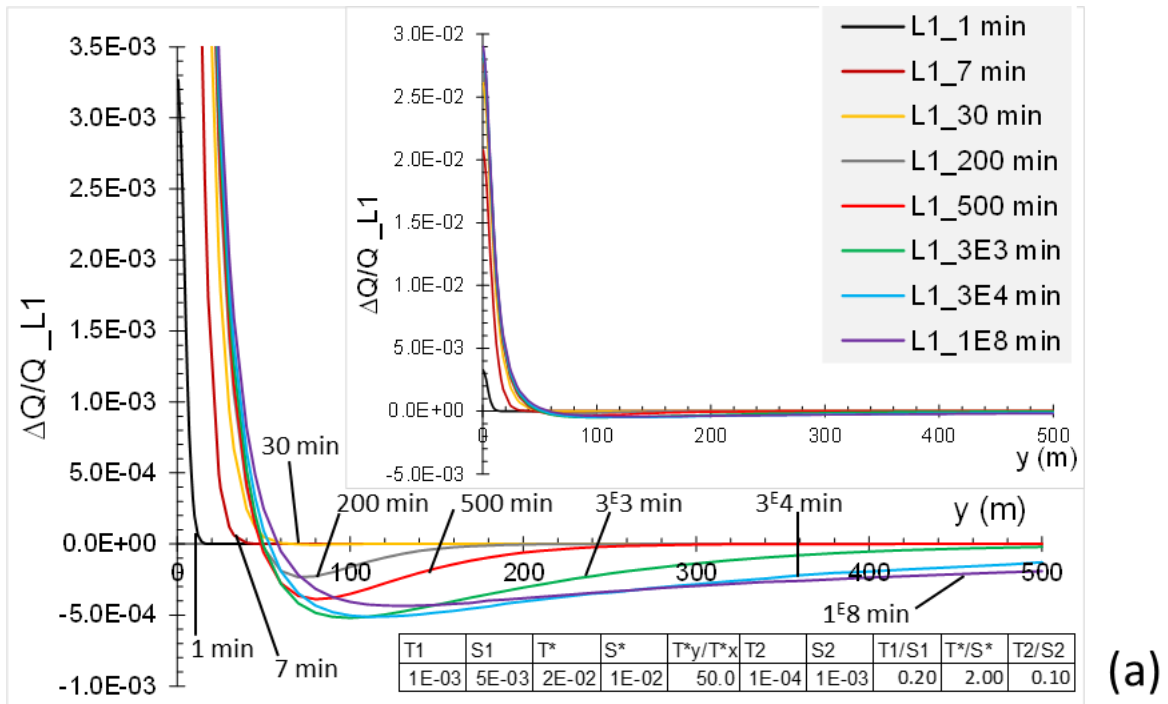


Figure 9

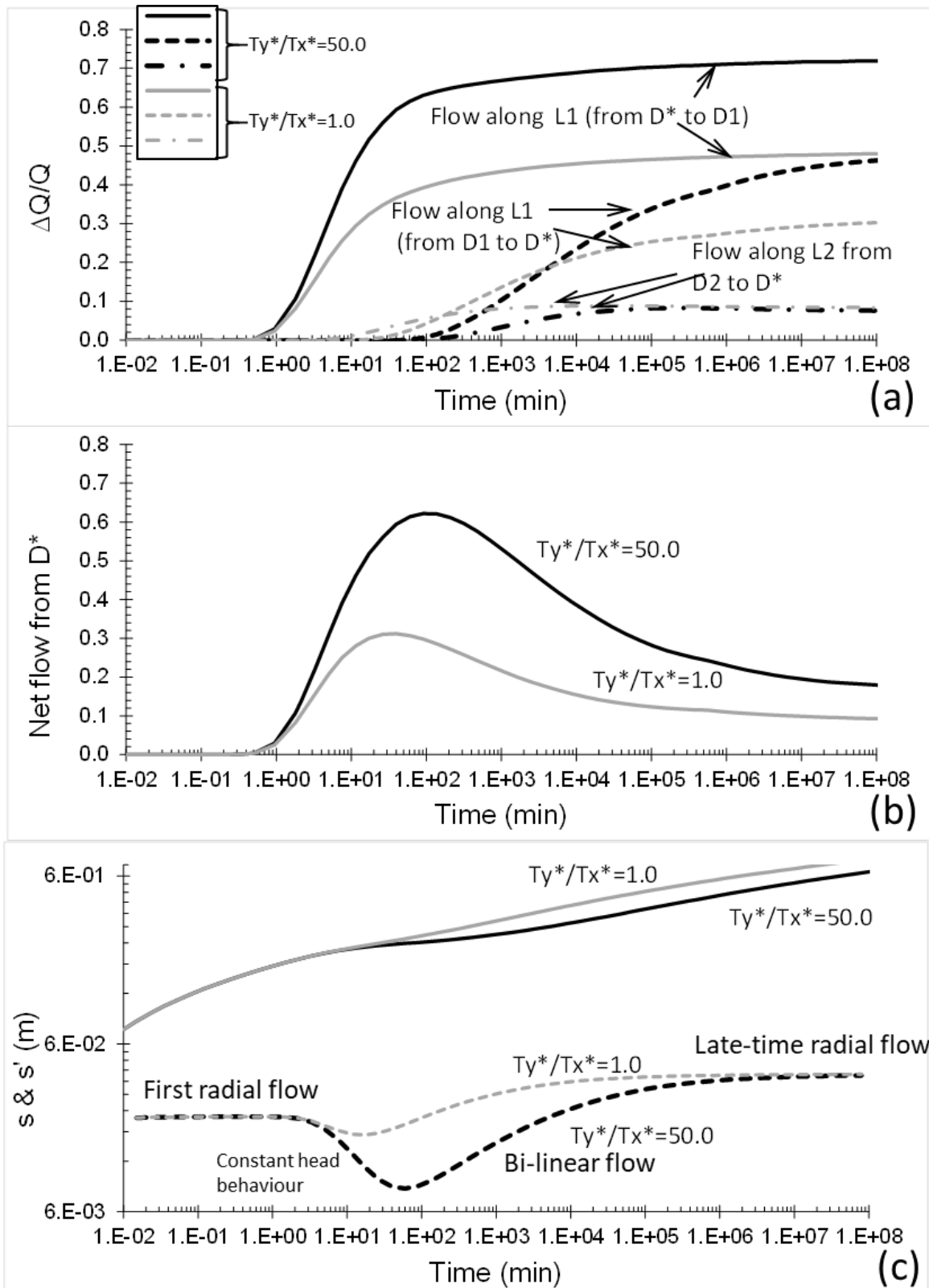


Figure 10

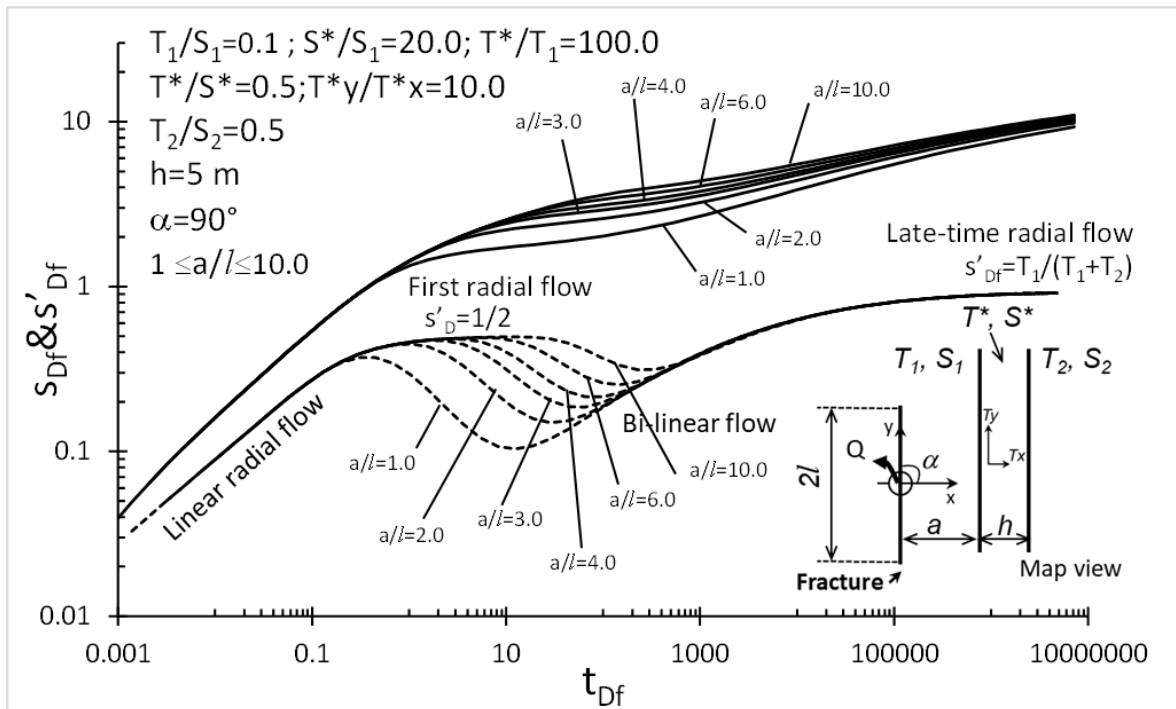
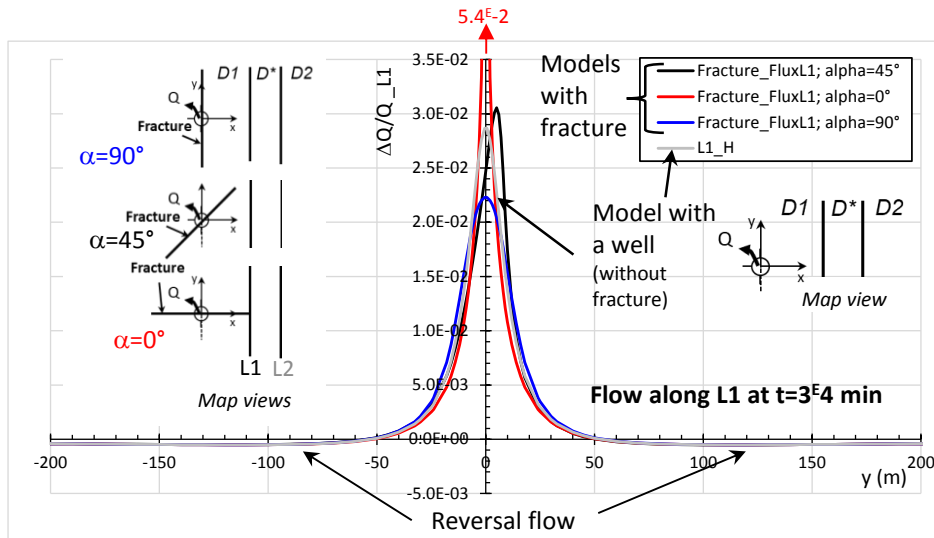
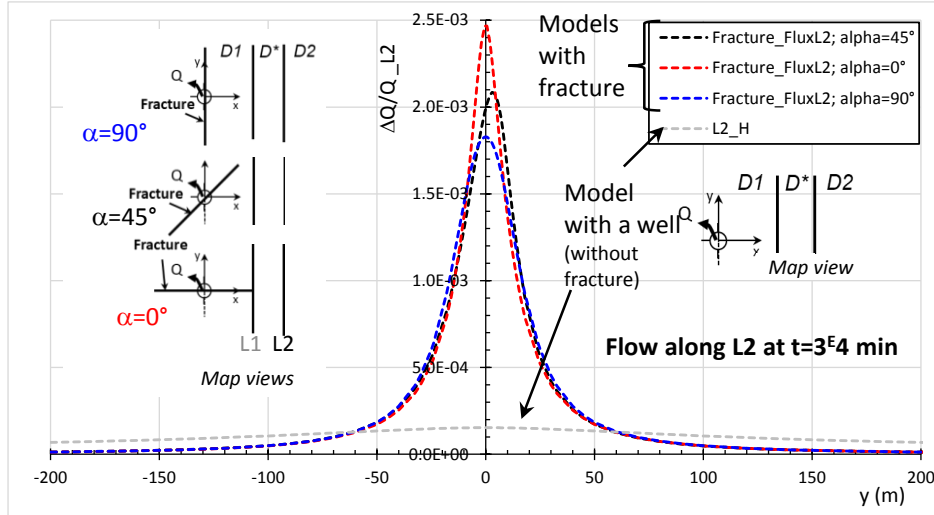


Figure 11

984



(a)



(b)

Figure 12

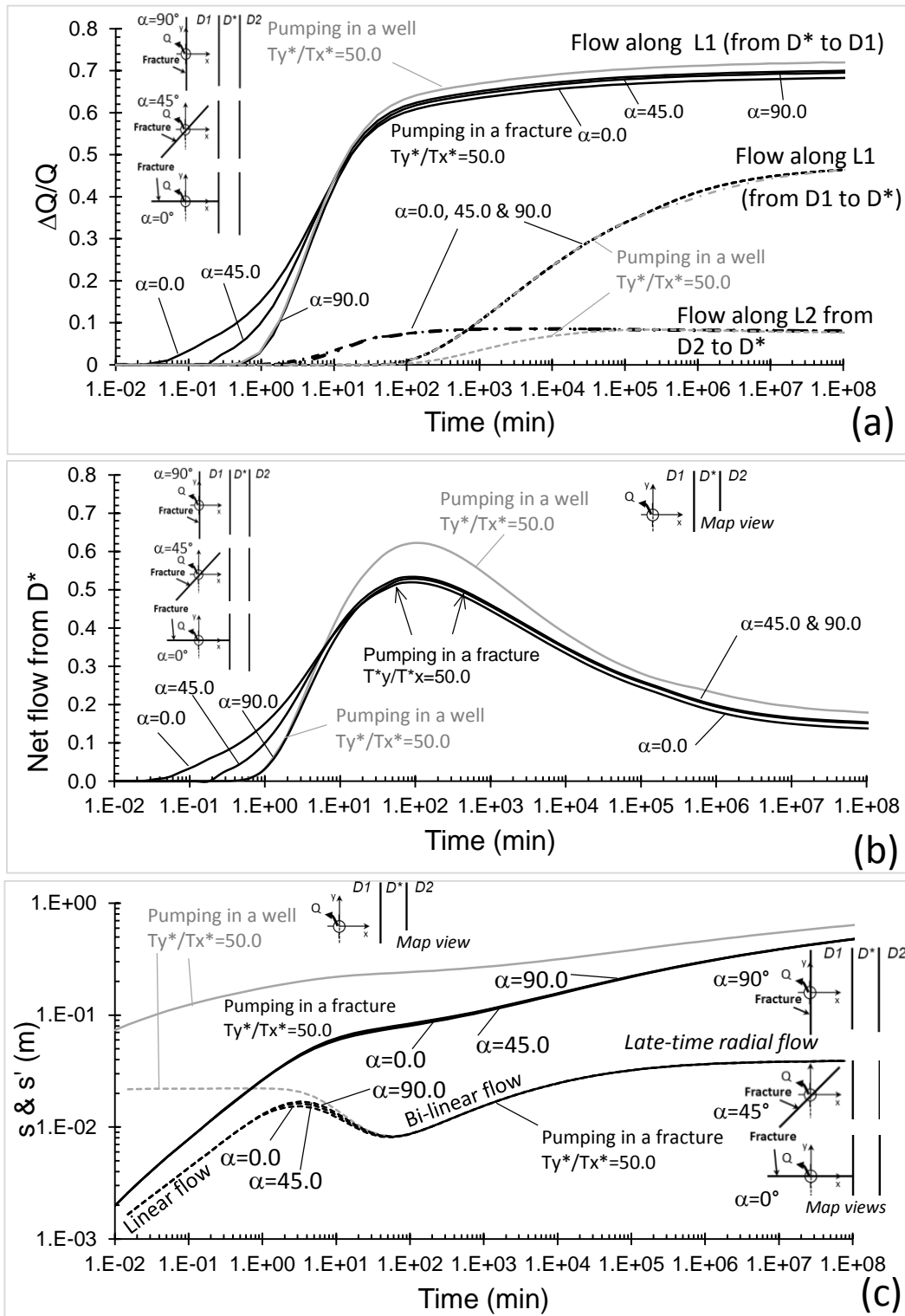


Figure 13